

Low-Altitude ISAC with Rotatable Active and Passive Arrays

Ziyuan Zheng, Qingqing Wu, Yanze Zhu, Honghao Wang, Ying Gao, Wen Chen, and Jian Xiong

Abstract—This paper investigates a low-altitude integrated sensing and communication (ISAC) system that leverages cooperative rotatable active and passive arrays. We consider a downlink scenario where a base station (BS) with an active rotatable array serves multiple communication users and senses low-altitude targets, assisted by a rotatable reconfigurable intelligent surface (RIS). A rotation-aware geometry-based multipath model is developed to capture the impact of three-dimensional (3D) array orientations on both steering vectors and direction-dependent element gains. On this basis, we formulate a new optimization problem that maximizes the downlink sum rate subject to a transmit power budget, RIS unit-modulus constraints, mechanical rotation limits, and a sensing beampattern mean-squared-error (MSE) constraint. To address the resulting highly non-convex problem, we propose a penalty-based alternating-optimization (AO) framework that alternately updates the BS precoder, RIS phase shifts, and BS/RIS array rotation angles. The three blocks are efficiently handled via a convex optimization method based on quadratic-transform (QT) and majorization-minimization (MM), Riemannian conjugate gradient (RCG) on the unit-modulus manifold, and projected gradient descent (PGD) with Barzilai–Borwein step sizes, respectively. Numerical results in low-altitude geometries demonstrate that the proposed jointly rotatable BS–RIS architecture achieves significant sum-rate gains over fixed or partially rotatable baselines while guaranteeing sensing requirements, especially with directional antennas and in interference-limited regimes.

Index Terms—Low-altitude wireless networks (LAWN), integrated sensing and communication (ISAC), rotatable array (RA), reconfigurable intelligent surface (RIS).

I. INTRODUCTION

Low-altitude wireless networks (LAWNs) are emerging as a key component of next-generation intelligent infrastructures, interconnecting uncrewed aerial vehicles (UAVs), low-altitude platform stations, aerial robots, and connected ground terminals in the three-dimensional (3D) airspace below a few kilometers [1]–[4]. Typical LAWN applications, such as aerial surveillance, disaster response, smart-city sensing, and low-altitude traffic management, rely not only on reliable broadband connectivity, but also on accurate situational awareness of dynamic low-altitude objects. This naturally calls for integrated sensing and communication (ISAC) designs that can jointly support data transmission and high-resolution sensing within complex, rapidly changing airspace environments [5], [6]. Compared with conventional terrestrial cellular systems, LAWNs must cope with fast-varying spatial

Z. Zheng, Q. Wu, Y. Zhu, H. Wang, Y. Gao, W. Chen, and J. Xiong are with the Department of Electronic Engineering, Shanghai Jiao Tong University, 200240, China (e-mail: {zhengziyuan2024, qingqingwu, yanzezhu, hhwang, yinggao, wenchen, xjarrow}@sjtu.edu.cn). (Corresponding author: Qingqing Wu.)

geometries and require shaping radio signals to illuminate aerial targets with stringent size–weight–power constraints and capture their reflections, which make efficient ISAC-oriented signal processing particularly challenging.

Multiple-input multiple-output (MIMO) technology and advanced precoding have long been recognized as key tools to exploit spatial degrees of freedom in wireless systems [7], [8]. MIMO systems provide significant gains in beamforming, spatial multiplexing, and diversity by leveraging independent or quasi-independent channel fading, thereby significantly improving spectral efficiency and link reliability. However, in classical designs, antenna arrays are fixed in position and orientation, limiting spatial control to electronic beamforming. For LAWNs, where users and targets are distributed in full 3D and may move at low altitude with complex trajectories, purely electronic beamforming is often not sufficient: system performance becomes strongly dependent on the relative 3D geometry among the base station (BS), scatterers, and low-altitude objects. This motivates the exploitation of geometry-aware architectures that can reshape both the propagation environment and the array response itself for LAWN-specific ISAC.

Reconfigurable intelligent surfaces (RISs) offer a promising approach to tailor the wireless environment via nearly passive phase-shift elements that reflect incident signals toward desired directions [9]–[11]. RIS-aided systems have been extensively investigated for coverage enhancement, interference mitigation, and energy-efficient MIMO operation. More recently, in addition to communication, RIS has been shown to improve wireless sensing, including target detection and localization, by redirecting illumination toward non-line-of-sight (NLoS) targets or acting as a passive reflector from favorable angles, thereby enriching spatial diversity [12]–[14]. In parallel, movable antennas (MA) has recently been proposed to further enhance spatial flexibility by allowing antenna elements or arrays to change their positions within a small region [15]–[18], enabling substantial gains in diversity, multiplexing, and interference management [19], and have been extended to multicast scenarios [20], as well as to two-timescale designs exploiting statistical channel state information (CSI) [21]. These works demonstrate that adding mechanical degrees of freedom to electronic beamforming can significantly improve performance.

However, most existing MA- or RIS-related works treat antenna movement or passive phase control in isolation [22], and their ISAC designs for LAWN-like geometries are much less explored: existing ISAC designs typically assume fixed arrays and do not exploit low-altitude 3D geometry control to

shape the transmit beampattern and the multiuser downlink channels simultaneously [23]. Furthermore, the mechanical flexibility in the MA literature is typically modeled as small-scale position changes within a local region. In contrast, realistic low-altitude platforms (e.g., UAV-mounted arrays or rooftop BS panels) can be designed to support rotation of the entire active or passive array via low-cost mechanical actuators [24]. Such rotatable arrays (RA) can jointly adjust their boresight directions, element coordinates, and directional gains, offering a distinct and practically relevant form of geometry control [25]. In summary, RIS-aided ISAC designs that consider rotatable passive arrays and their coupling with active-array rotations at the BS have yet to be systematically studied, especially under explicit constraints on the similarity of sensing beam patterns. As a result, the fundamental question of how to jointly design rotatable active and passive arrays, RIS phase shifts, and multiuser transmit beamforming for low-altitude ISAC remains open.

Motivated by these observations, this paper investigates a low-altitude ISAC architecture with cooperatively rotatable active and passive arrays. We consider a downlink LAWN scenario where a BS equipped with an active rotatable array simultaneously serves multiple single-antenna ground users and senses low-altitude targets in monostatic mode, assisted by a rotatable RIS termed passive array. Both arrays can rotate in 3D, and the resulting orientations jointly affect (i) the element coordinates in the steering vectors and (ii) direction-dependent element/array gains through a practical directivity model. Based on the rotation-aware channel model, we explicitly couple communication and sensing performance and formulate a joint design problem that maximizes the sum rate subject to a sensing constraint, a BS transmit-power budget, and mechanical rotation limits at both the BS and RIS, with design variables given by the BS ISAC precoder, the RIS phase-shift vector, and the 3D rotation angles of the two arrays.

The main contributions of this work are summarized as

- We propose a LAWN-oriented ISAC architecture in which a rotatable active BS array cooperates with a rotatable passive RIS array to serve multiple communication users and jointly sense low-altitude targets. We develop a rotation-aware 3D multipath channel model that captures both phase shifts from rotated antenna/element positions and direction-dependent antenna/element directional radiation pattern gains. Based on this model, we derive closed-form expressions for the multiuser downlink SINR and the monostatic sensing beampattern, and formulate a new optimization problem that maximizes the communication sum rate under a sensing beampattern mean-squared-error (MSE) constraint, power budget on the BS, unit-modulus constraint on the RIS and mechanical rotation bounds on RA, thereby revealing mechanical rotations as additional spatial degrees of freedom for LAWN ISAC.
- We convert the constrained ISAC design into a penalized formulation with a hinge penalty on the sensing MSE and develop an alternating optimization (AO) framework that iteratively updates the BS precoder, RIS phase shifts,

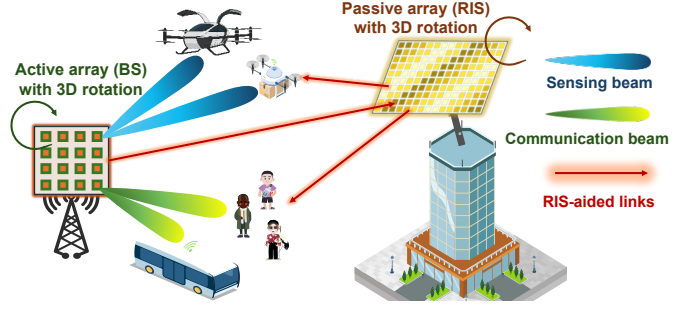


Fig. 1. Illustration of a low-altitude ISAC system with rotatable active and passive arrays.

and array rotations. For the BS precoding block, we combine the quadratic transform (QT) and the Lagrangian dual transform (LDT) with a majorization–minimization (MM) step to obtain a tractable quadratic-constrained quadratic program (QCQP) subproblem that admits a closed-form water-filling-like update. For the RIS block, we exploit the complex-circle manifold structure and design an efficient Riemannian conjugate gradient (RCG) algorithm. For the rotation block, we derive closed-form gradients of both SINR and beampattern MSE with respect to the BS/RIS Euler angles and employ a projected gradient descent (PGD) method with Barzilai–Borwein initialization and Armijo backtracking.

- We conduct extensive simulations using LAWN-inspired 3D geometries and compare the proposed design with several baselines, including only BS rotation, only RIS rotation, fully fixed arrays, and non-RIS configurations. The results show that the jointly rotatable BS–RIS architecture provides substantial sum-rate gains under the same sensing MSE constraint across varying transmit powers, antenna array sizes, and user densities. The gains are further amplified with realistic directional element patterns, highlighting the importance of aligning the array boresights and main lobes with both user and target directions in a low-altitude 3D space.

The rest of the paper is structured as follows: Section II introduces the system model and problem formulation. Section III presents proposed algorithm. Section IV presents the numerical results, and Section V concludes the paper.

II. SYSTEM MODEL AND PROBLEM FORMULATION

We consider a downlink RA-enabled ISAC system, as shown in Fig. 1, where a base station (BS) uses an *active* rotatable uniform planar array (UPA) with M transmit antennas to serve K single-antenna users while sensing multiple targets in a monostatic mode; at the same time, a *passive* rotatable UPA RIS with N reflecting elements assists both tasks. In addition to active transmit beamforming at the BS and passive phase shifts at the RIS, both arrays can rotate in 3D. These rotations steer the array boresights and reshape the array response to improve, or balance, communication and sensing performance.

A. Array Geometry and Rotations

We adopt a global right-handed Cartesian coordinate system (CCS) $\mathcal{F}_0 = (O, x, y, z)$. The BS employs a co-located transmit/receive UPA with size $M = M_x \times M_y$, and the RIS is a UPA with size $N = N_x \times N_y$. Let $\bar{d}_m^B \in \mathbb{R}^3$ and $\bar{d}_n^R \in \mathbb{R}^3$ denote the *unrotated* local coordinates of the m -th BS transmit antenna and the n -th RIS reflecting element, respectively, and let d_0^B and d_0^R be their array centers in \mathcal{F}_0 . Both BS and RIS employ a motorized mechanism to rotate the arrays as a whole. Based on the system's ISAC requirements, the proper rotation angles are determined by a central control center, which is connected to the motor controllers via fiber links.

Each array rotates as a rigid body through Euler angles

$$\mathbf{r}^B \triangleq [\zeta_x^B, \zeta_y^B, \zeta_z^B]^T, \quad (1a)$$

$$\mathbf{r}^R \triangleq [\zeta_x^R, \zeta_y^R, \zeta_z^R]^T, \quad (1b)$$

respectively, in their local CCS. The corresponding rotation matrix generated by \mathbf{r}^A , where we define $A \in \{B, R\}$ for brevity, represents the rotations about their local axis with the standard intrinsic z - y - x convention and is given by

$$\mathbf{R}(\zeta_x^A, \zeta_y^A, \zeta_z^A) = \mathbf{R}_x(\zeta_x^A) \mathbf{R}_y(\zeta_y^A) \mathbf{R}_z(\zeta_z^A), \quad (2)$$

where the rotation matrices on each axis are defined by

$$\mathbf{R}_x(\zeta_x^A) = \begin{bmatrix} 1 & 0 & 0 \\ 0 & \cos \zeta_x^A & -\sin \zeta_x^A \\ 0 & \sin \zeta_x^A & \cos \zeta_x^A \end{bmatrix}, \quad (3a)$$

$$\mathbf{R}_y(\zeta_y^A) = \begin{bmatrix} \cos \zeta_y^A & 0 & \sin \zeta_y^A \\ 0 & 1 & 0 \\ -\sin \zeta_y^A & 0 & \cos \zeta_y^A \end{bmatrix}, \quad (3b)$$

$$\mathbf{R}_z(\zeta_z^A) = \begin{bmatrix} \cos \zeta_z^A & -\sin \zeta_z^A & 0 \\ \sin \zeta_z^A & \cos \zeta_z^A & 0 \\ 0 & 0 & 1 \end{bmatrix}. \quad (3c)$$

The *rotated* antenna or element coordinates in \mathcal{F}_0 are then

$$\mathbf{d}_m^B(\mathbf{r}^B) = \mathbf{d}_0^B + \mathbf{R}(\mathbf{r}^B) \bar{d}_m^B, \quad (4a)$$

$$\mathbf{d}_n^R(\mathbf{r}^R) = \mathbf{d}_0^R + \mathbf{R}(\mathbf{r}^R) \bar{d}_n^R. \quad (4b)$$

Note that rotations affect both (i) the position of antennas or elements in the phase term of the steering vector and (ii) the directivity gain of radiation patterns for the arrays, which are jointly captured through direction- and position-dependent gains introduced in the following channel modeling.

B. Direction and Steering Vectors

For a far-field direction parameterized by an elevation-azimuth pair (ϑ, φ) with elevation from the xOy plane and azimuth from the x -axis, define the direction vector

$$\mathbf{u}(\vartheta, \varphi) \triangleq [\cos \vartheta \cos \varphi, \cos \vartheta \sin \varphi, \sin \vartheta]^T. \quad (5)$$

We adopt the geometry channel model to characterize the wireless propagation environment. Let $\mathcal{Q}_k = \{1, \dots, Q_k\}$, $\mathcal{L}_k = \{1, \dots, L_k\}$, and $\mathcal{P} = \{1, \dots, P\}$ denote the set of propagation paths between the k -th user and the BS, between the k -th user and the RIS, and between the RIS and the BS, respectively; specifically, we assume that the first paths in \mathcal{Q}_k , \mathcal{L}_k , and \mathcal{P} , corresponding to $l_k = 1$, $q_k = 1$ and

$p = 1$, respectively, are the line-of-sight (LoS) paths, while the remaining $L_k - 1$, $Q_k - 1$ and $P - 1$ are the non-LoS paths. For the targeted sensing area with low-altitude UAVs, we consider merely the single LoS path with a potential reflected echo signal in each desired direction.

Accordingly, we use the following indexed notational short-hands for distinct BS-user (BU), RIS-BS (RB), BS-RIS (BR), and RIS-user (RU) links, respectively

$$\mathbf{u}_{k,l}^{\text{BU}} = [\cos(\vartheta_{k,l}^{\text{BU}}) \cos(\varphi_{k,l}^{\text{BU}}), \cos(\vartheta_{k,l}^{\text{BU}}) \sin(\varphi_{k,l}^{\text{BU}}), \sin(\vartheta_{k,l}^{\text{BU}})]^T, \quad (6a)$$

$$\mathbf{u}_p^{\text{RB}} = [\cos(\vartheta_p^{\text{RB}}) \cos(\varphi_p^{\text{RB}}), \cos(\vartheta_p^{\text{RB}}) \sin(\varphi_p^{\text{RB}}), \sin(\vartheta_p^{\text{RB}})]^T, \quad (6b)$$

$$\mathbf{u}_p^{\text{BR}} = [\cos(\vartheta_p^{\text{BR}}) \cos(\varphi_p^{\text{BR}}), \cos(\vartheta_p^{\text{BR}}) \sin(\varphi_p^{\text{BR}}), \sin(\vartheta_p^{\text{BR}})]^T, \quad (6c)$$

$$\mathbf{u}_{k,q}^{\text{RU}} = [\cos(\vartheta_{k,q}^{\text{RU}}) \cos(\varphi_{k,q}^{\text{RU}}), \cos(\vartheta_{k,q}^{\text{RU}}) \sin(\varphi_{k,q}^{\text{RU}}), \sin(\vartheta_{k,q}^{\text{RU}})]^T. \quad (6d)$$

The associated steering vectors, jointly parameterized by the coordinates of the rotated elements in (4) and the direction vectors in (6), can be given by

$$\mathbf{t}_{k,l}^{\text{BU}}(\mathbf{r}^B) = [e^{j\frac{2\pi}{\lambda}(\mathbf{u}_{k,l}^{\text{BU}})^T \mathbf{d}_1^B(\mathbf{r}^B)}, \dots, e^{j\frac{2\pi}{\lambda}(\mathbf{u}_{k,l}^{\text{BU}})^T \mathbf{d}_M^B(\mathbf{r}^B)}]^T, \quad (7a)$$

$$\mathbf{t}_p^{\text{BR}}(\mathbf{r}^B) = [e^{j\frac{2\pi}{\lambda}(\mathbf{u}_p^{\text{BR}})^T \mathbf{d}_1^B(\mathbf{r}^B)}, \dots, e^{j\frac{2\pi}{\lambda}(\mathbf{u}_p^{\text{BR}})^T \mathbf{d}_M^B(\mathbf{r}^B)}]^T, \quad (7b)$$

$$\mathbf{t}_p^{\text{RB}}(\mathbf{r}^R) = [e^{j\frac{2\pi}{\lambda}(\mathbf{u}_p^{\text{RB}})^T \mathbf{d}_1^R(\mathbf{r}^R)}, \dots, e^{j\frac{2\pi}{\lambda}(\mathbf{u}_p^{\text{RB}})^T \mathbf{d}_M^R(\mathbf{r}^R)}]^T, \quad (7c)$$

$$\mathbf{t}_{k,q}^{\text{RU}}(\mathbf{r}^B) = [e^{j\frac{2\pi}{\lambda}(\mathbf{u}_{k,q}^{\text{RU}})^T \mathbf{d}_1^R(\mathbf{r}^R)}, \dots, e^{j\frac{2\pi}{\lambda}(\mathbf{u}_{k,q}^{\text{RU}})^T \mathbf{d}_N^R(\mathbf{r}^R)}]^T. \quad (7d)$$

Similarly, for a target direction (ϑ_a, φ_a) within the target sensing area \mathcal{A} , the direction steering vectors for BS-target (BT) and RIS-target (RT) links can be respectively given by

$$\mathbf{u}_a^{\text{BT}} = [\cos(\vartheta_a^{\text{BT}}) \cos(\varphi_a^{\text{BT}}), \cos(\vartheta_a^{\text{BT}}) \sin(\varphi_a^{\text{BT}}), \sin(\vartheta_a^{\text{BT}})]^T, \quad (8a)$$

$$\mathbf{u}_a^{\text{RT}} = [\cos(\vartheta_a^{\text{RT}}) \cos(\varphi_a^{\text{RT}}), \cos(\vartheta_a^{\text{RT}}) \sin(\varphi_a^{\text{RT}}), \sin(\vartheta_a^{\text{RT}})]^T, \quad (8b)$$

and

$$\mathbf{t}_a^{\text{BT}}(\mathbf{r}^B) = [e^{j\frac{2\pi}{\lambda}(\mathbf{u}_a^{\text{BT}})^T \mathbf{d}_1^B(\mathbf{r}^B)}, \dots, e^{j\frac{2\pi}{\lambda}(\mathbf{u}_a^{\text{BT}})^T \mathbf{d}_M^B(\mathbf{r}^B)}]^T, \quad (9a)$$

$$\mathbf{t}_a^{\text{RT}}(\mathbf{r}^B) = [e^{j\frac{2\pi}{\lambda}(\mathbf{u}_a^{\text{RT}})^T \mathbf{d}_1^R(\mathbf{r}^R)}, \dots, e^{j\frac{2\pi}{\lambda}(\mathbf{u}_a^{\text{RT}})^T \mathbf{d}_N^R(\mathbf{r}^R)}]^T. \quad (9b)$$

As shown in (7) and (9), array rotations, which generate position-dependent effects on the steering vector's phase term, can be exploited to reshape channel responses.

C. Rotation-Aware Multipath Channels

To capture rotation-dependent directivity in the radiation pattern of BS and RIS arrays, we include non-negative gain terms $G^B(\mathbf{r}^B)$ and $G^R(\mathbf{r}^R)$, which model directional antenna and element patterns under rotation. Let $\bar{\mathbf{n}} = [0, 0, 1]^T$ and

$$\mathbf{n}(\mathbf{r}^A) = \mathbf{R}(\mathbf{r}^A) \bar{\mathbf{n}} \quad (10)$$

be the unrotated and rotated array boresight, respectively, we adopt a practical directivity model

$$G^B(\mathbf{r}^B; \mathbf{u}^B) = \begin{cases} -G_0^B(\mathbf{n}^T(\mathbf{r}^B) \mathbf{u}^B)^{p^B}, & \text{if } \mathbf{n}^T(\mathbf{r}^B) \mathbf{u}^B < 0, \\ 0, & \text{otherwise,} \end{cases} \quad (11a)$$

$$G^R(\mathbf{r}^R; \mathbf{u}^R) = \begin{cases} -G_0^R(\mathbf{n}^T(\mathbf{r}^R) \mathbf{u}^R)^{p^R}, & \text{if } \mathbf{n}^T(\mathbf{r}^R) \mathbf{u}^R < 0, \\ 0, & \text{otherwise,} \end{cases} \quad (11b)$$

where G_0^B and G_0^R denotes the maximum gain achieved when the signal aligns with the boresight, and p^B and p^R are the directivity factors controlling the main-lobe width, following from directivity normalization over the full sphere. Then, with given numbers of resolvable paths L_k , P , and Q_k , and small-scale complex gains $a_{k,l}$, b_p , and $c_{k,q}$ that absorb path loss and fading, the BS-to-user channel $\mathbf{h}_k(\mathbf{r}^B) \in \mathbb{C}^M$, BS-to-RIS channel $\mathbf{B}(\mathbf{r}^B, \mathbf{r}^R) \in \mathbb{C}^{M \times N}$, and RIS-to-user channel $\mathbf{g}_k(\mathbf{r}^R) \in \mathbb{C}^N$ are respectively expressed as

$$\mathbf{h}_k(\mathbf{r}^B) = \sum_{l=1}^{L_k} a_{k,l} \sqrt{G_{k,l}^B(\mathbf{r}^B)} \mathbf{t}_{k,l}^{\text{BU}}(\mathbf{r}^B) \quad (12a)$$

$$\begin{aligned} \mathbf{B}(\mathbf{r}^B, \mathbf{r}^R) = & \sum_{p=1}^P b_p \sqrt{G_{k,p}^B(\mathbf{r}^B, \mathbf{r}^R) G_{k,p}^R(\mathbf{r}^B, \mathbf{r}^R)} \\ & \times \mathbf{t}_p^{\text{BR}}(\mathbf{r}^B) (\mathbf{t}_p^{\text{RB}}(\mathbf{r}^R))^H \end{aligned} \quad (12b)$$

$$\mathbf{g}_k(\mathbf{r}^R) = \sum_{q=1}^{Q_k} c_{k,q} \sqrt{G_{k,q}^R(\mathbf{r}^R)} \mathbf{t}_{k,q}^{\text{RU}}(\mathbf{r}^R). \quad (12c)$$

Taking into account direct and cascaded RIS-enabled links, the effective composite channel from BS to the k -th user is

$$\mathbf{f}_k(\mathbf{r}^B, \mathbf{r}^R, \boldsymbol{\theta}) = \mathbf{h}_k(\mathbf{r}^B) + \mathbf{B}(\mathbf{r}^B, \mathbf{r}^R) \text{diag}(\boldsymbol{\theta}) \mathbf{g}_k(\mathbf{r}^R), \quad (13)$$

where $\boldsymbol{\theta} = [\theta_1, \dots, \theta_N]^T$ collects the RIS reflecting phase shift coefficients, typically being passive with $|\theta_n| = 1$. Similarly, for sensing, define the effective steering toward a target direction (ϑ_a, φ_a) as

$$\begin{aligned} \mathbf{f}_{S,a}(\mathbf{r}^B, \mathbf{r}^R, \boldsymbol{\theta}) = & \sqrt{G_a^B(\mathbf{r}^B)} a_a \mathbf{t}_a^{\text{BT}}(\mathbf{r}^B) + \mathbf{B}(\mathbf{r}^B, \mathbf{r}^R) \text{diag}(\boldsymbol{\theta}) \\ & \times \sqrt{G_a^R(\mathbf{r}^R)} c_a \mathbf{t}_a^{\text{RT}}(\mathbf{r}^R) \end{aligned} \quad (14)$$

D. Transmit Signal, Communication SINR, and Sensing MSE

The BS transmits an ISAC signal

$$\mathbf{x} = \mathbf{W}_C \mathbf{s}_C + \mathbf{W}_S \mathbf{s}_S, \quad (15)$$

where $\mathbf{W}_C = [\mathbf{w}_1, \dots, \mathbf{w}_K] \in \mathbb{C}^{M \times K}$ collects K communication beams, $\mathbf{W}_S \in \mathbb{C}^{M \times M}$ contains dedicated sensing beams, $\mathbf{s}_C = [s_1, \dots, s_K]^T$ denotes the communication symbols, and \mathbf{s}_S denotes the sensing signals, with $\mathbb{E}[\mathbf{s}_S \mathbf{s}_S^H] = \mathbf{I}_M$, $\mathbf{s}_C \sim \mathcal{CN}(\mathbf{0}, \mathbf{I}_K)$, and $\mathbb{E}[\mathbf{s}_S \mathbf{s}_C^H] = \mathbf{0}$. Let $\mathbf{W} \triangleq [\mathbf{W}_C, \mathbf{W}_S]$ denotes the BS ISAC transmit beamforming matrix, $\mathbf{s} \triangleq [\mathbf{s}_C^T, \mathbf{s}_S^T]^T$, the received signal at the communication user k is written as

$$y_k = \mathbf{f}_k^H(\mathbf{r}^B, \mathbf{r}^R, \boldsymbol{\theta}) \mathbf{W} \mathbf{s} \quad (16a)$$

$$\begin{aligned} &= \mathbf{f}_k^H(\mathbf{r}^B, \mathbf{r}^R, \boldsymbol{\theta}) \mathbf{w}_k s_k + \sum_{i=1, i \neq k}^K \mathbf{f}_k^H(\mathbf{r}^B, \mathbf{r}^R, \boldsymbol{\theta}) \mathbf{w}_i x_i \\ &+ \mathbf{f}_k^H(\mathbf{r}^B, \mathbf{r}^R, \boldsymbol{\theta}) \mathbf{W}_S \mathbf{s}_S + n_k, \end{aligned} \quad (16b)$$

where $n_k \sim \mathcal{CN}(0, \sigma_k^2)$ is the complex additive white Gaussian noise. Taking further $\mathbf{W} \triangleq [\mathbf{w}_1, \dots, \mathbf{w}_{K+N}]$, where \mathbf{w}_i is the i -th column of \mathbf{W} , the SINR of the k -th user is

$$\text{SINR}_k = \frac{|\mathbf{f}_k^H(\mathbf{r}^B, \mathbf{r}^R, \boldsymbol{\theta}) \mathbf{w}_k|^2}{\sum_{i=1, i \neq k}^{K+N} |\mathbf{f}_k^H(\mathbf{r}^B, \mathbf{r}^R, \boldsymbol{\theta}) \mathbf{w}_i|^2 + \sigma_k^2}, \quad (17)$$

For sensing, the transmit beam pattern toward (ϑ_a, φ_a) is

$$\mathcal{P}(\vartheta_a, \varphi_a) = \mathbb{E}(|\mathbf{f}_{S,a}^H(\mathbf{r}^B, \mathbf{r}^R, \boldsymbol{\theta}) \mathbf{W} \mathbf{s}|^2) \quad (18a)$$

$$= \mathbf{f}_{S,a}^H(\mathbf{r}^B, \mathbf{r}^R, \boldsymbol{\theta}) \mathbf{W} \mathbf{W}^H \mathbf{f}_{S,a}(\mathbf{r}^B, \mathbf{r}^R, \boldsymbol{\theta}). \quad (18b)$$

Using (13) this expands to

$$\begin{aligned} &\mathcal{P}(\vartheta_a, \varphi_a) \\ &= (\mathbf{t}_a^{\text{BT}}(\mathbf{r}^B))^H \mathbf{W} \mathbf{W}^H \mathbf{t}_a^{\text{BT}}(\mathbf{r}^B) + 2\sqrt{G_a^B(\mathbf{r}^B) G_a^R(\mathbf{r}^R)} \\ &\quad \times \text{Re}\{(\mathbf{t}_a^{\text{BT}}(\mathbf{r}^B))^H \mathbf{W} \mathbf{W}^H \mathbf{B}(\mathbf{r}^B, \mathbf{r}^R) \text{diag}(\boldsymbol{\theta}) \mathbf{t}_a^{\text{RT}}(\mathbf{r}^R)\} \\ &\quad + \sqrt{G_a^B(\mathbf{r}^B) G_a^R(\mathbf{r}^R)} (\mathbf{B}(\mathbf{r}^B, \mathbf{r}^R) \text{diag}(\boldsymbol{\theta}) \mathbf{t}_a^{\text{RT}}(\mathbf{r}^R))^H \\ &\quad \times \mathbf{W} \mathbf{W}^H \mathbf{B}(\mathbf{r}^B, \mathbf{r}^R) \text{diag}(\boldsymbol{\theta}) \mathbf{t}_a^{\text{RT}}(\mathbf{r}^R). \end{aligned} \quad (19)$$

Given a discretized grid $\{(\vartheta_a, \varphi_a)\}_{a=1}^A, a \in \{1, \dots, A\}$ with A sampled points in total, which samples the azimuth and elevation angular domain over the target sensing area \mathcal{A} , along with the desired beam pattern $\mathcal{P}_d(\vartheta_a, \varphi_a)$, the mean squared error (MSE) between \mathcal{P} and \mathcal{P}_d to evaluate the similarity of the sensing beam pattern is defined as []

$$\text{MSE} = \frac{1}{A} \sum_{a=1}^A |\mathcal{P}(\vartheta_a, \varphi_a; \mathbf{r}^B, \mathbf{r}^R, \boldsymbol{\theta}, \mathbf{W}) - \mathcal{P}_d(\vartheta_a, \varphi_a)|^2. \quad (20)$$

A typical ideal desired beam pattern is given by

$$\mathcal{P}_d(\vartheta_a, \varphi_a) = \begin{cases} 1, a \in \mathcal{T} \\ 0, \text{otherwise} \end{cases} \quad (21)$$

where \mathcal{T} is the set of focused grid points in the region \mathcal{A} .

E. Problem Formulation

Accordingly, we jointly optimize the BS and RIS rotations, the RIS phase shifts, and the BS transmit beamforming to maximize the sum-rate performance for communication with the guaranteed sensing requirement on the beam pattern MSE

$$(P1) : \max_{\mathbf{r}^B, \mathbf{r}^R, \boldsymbol{\theta}, \mathbf{W}} \sum_{k=1}^K \log_2 (1 + \text{SINR}_k) \quad (22a)$$

$$\text{s.t. } \text{MSE} \leq \eta_{\text{th}} \quad (22b)$$

$$\|\mathbf{W}\|_F^2 = \text{Tr}(\mathbf{W} \mathbf{W}^H) \leq P_B, \quad (22c)$$

$$|\theta_n| = 1, \forall n \in \mathcal{N}, \quad (22d)$$

$$\zeta_i^B \in [\zeta_{i,\min}^B, \zeta_{i,\max}^B], i \in \{x, y, z\}, \quad (22e)$$

$$\zeta_i^R \in [\zeta_{i,\min}^R, \zeta_{i,\max}^R], i \in \{x, y, z\}, \quad (22f)$$

where η_{th} in (22b) is the maximum allowed sensing MSE, P_B in (22c) is the BS power budget, the unit-modulus constraint (23d) enforces a passive RIS, and the box constraints (22e) and (22f) capture mechanical limits of the array rotations at BS and RIS, respectively.

From the formulated problem, we observe that the rotation variables $(\mathbf{r}^B, \mathbf{r}^R)$ provide a *geometric* control that affects the steering vectors and directive gain, thereby complementing the *electromagnetic* control offered by active and passive beamforming at the RIS and BS arrays; consequently, jointly optimizing these blocks yields a significant DoF for low-altitude ISAC. However, (P1) is highly non-convex due to unit-modulus constraints, rotation-induced nonlinearities in the steering vector and directive gain, and the coupling among \mathbf{r}^B , \mathbf{r}^R , $\boldsymbol{\theta}$, and \mathbf{W} in both SINR and MSE expressions.

III. PROPOSED ALGORITHM

In this section, we convert (P1) to a penalized form and solve it by resorting to AO technique across three blocks: BS transmit beamforming \mathbf{W} , RIS passive beamforming $\boldsymbol{\theta}$, and array rotations $(\mathbf{r}^B, \mathbf{r}^R)$. The three subproblems are handled by a quadratic transform (QT) and a majorization-minimization (MM) step for \mathbf{W} , Riemannian optimization for $\boldsymbol{\theta}$, and the projection gradient-based method for $(\mathbf{r}^B, \mathbf{r}^R)$, respectively.

A. Penalty Method and AO Framework

The beam pattern similarity constraints (22b), with a high-order non-convex MSE expression, limit the feasible region and hinder the solution of (P1). To handle this difficulty, we incorporate (22b) into the objective function as a *hinge penalty* term, obtaining a more tractable reformulated problem

$$(P1.1) : \max_{\mathbf{r}^B, \mathbf{r}^R, \boldsymbol{\theta}, \mathbf{W}} \sum_{k=1}^K \log_2 (1 + \text{SINR}_k (\mathbf{r}^B, \mathbf{r}^R, \boldsymbol{\theta}, \mathbf{W})) - \rho \max\{\text{MSE} (\mathbf{r}^B, \mathbf{r}^R, \boldsymbol{\theta}, \mathbf{W}) - \eta_{\text{th}}, 0\} \quad (23)$$

s.t. (22c), (22d), (22e), (22f)

where the adjustable penalty parameter $\rho \geq 0$ penalizes violations of (22b) with the hinge penalty function $\max\{\text{MSE} - \eta_{\text{th}}, 0\}$. When $\rho \rightarrow \infty$, any solution $\{(\mathbf{r}^B)^*, (\mathbf{r}^R)^*, \boldsymbol{\theta}^*, \mathbf{W}^*\}$ of (P1.1) should meet the condition $\text{MSE} \leq \eta_{\text{th}}$, establishing the equivalence between (P1) and (P1.1). Since setting ρ large at the beginning renders this approach ineffective, we initialize ρ by a small value to find a good starting point, solve problem (P1.1) iteratively with gradually increased ρ , until $\text{MSE} \leq \eta_{\text{th}}$ holds and the objective function reaches the convergence criteria. ρ increases only when $\text{MSE} > \eta_{\text{th}}$ persists; once the constraint is satisfied, ρ is kept fixed to avoid unnecessary rate loss.

Even with fixed ρ , due to the non-concave objective function and the non-convex constraints with closely coupled variables, (P1.1) remains highly non-convex and challenging to solve directly. Nevertheless, observing that the problem becomes more tractable when optimizing one variable block at a time, we resort to the AO method: at each outer iteration, we cyclically optimize the transmit beamforming \mathbf{W} , the RIS phase shifts $\boldsymbol{\theta}$, and the array rotations $\{\mathbf{r}^B, \mathbf{r}^R\}$, while keeping the others fixed, as detailed in the following subsections.

B. QT- and MM-based Transmit Beamforming

With fixed $(\boldsymbol{\theta}, \mathbf{r}^B, \mathbf{r}^R)$, the subproblem optimizing \mathbf{W} reads

$$(P2) : \max_{\mathbf{W}} \sum_{k=1}^K \log_2 (1 + \text{SINR}_k (\mathbf{W})) - \rho \max\{\text{MSE} (\mathbf{W}) - \eta_{\text{th}}, 0\} \quad (24)$$

s.t. (22c),

where the SINR and MSE expressions reduce to

$$\text{SINR}_k (\mathbf{W}) = \frac{|\mathbf{f}_k^H \mathbf{w}_k|^2}{\sum_{i=1, i \neq k}^{K+M} |\mathbf{f}_k^H \mathbf{w}_i|^2 + \sigma_k^2}, \quad (25a)$$

$$\text{MSE} (\mathbf{W}) = \frac{1}{A} \sum_{a=1}^A \left| \|\mathbf{W}^H \mathbf{f}_{S,a}\|_2^2 - \mathcal{P}_{d,a} \right|^2. \quad (25b)$$

The power constraint (22c) is convex, and the non-concavity of (24) originates from the fractional SINR and fourth-order MSE expressions, which are sequentially tackled as follows.

1) *Sensing MSE term with MM-based second-order upper bound*: For brevity, let

$$g_a (\mathbf{W}) \triangleq (\|\mathbf{W}^H \mathbf{f}_{S,a}\|_2^2 - \mathcal{P}_{d,a})^2, \quad (26a)$$

$$= (\text{Tr}(\mathbf{W}^H \mathbf{S}_a \mathbf{W}) - \mathcal{P}_{d,a})^2, \quad (26b)$$

with the rank-one positive semi-definite matrix defined by

$$\mathbf{S}_a \triangleq \mathbf{f}_{S,a} \mathbf{f}_{S,a}^H \succeq 0, \quad (27)$$

we have the gradient of (26) being

$$\mathbf{G}_a (\mathbf{W}) \triangleq \nabla g_a (\mathbf{W}) \quad (28a)$$

$$= 4(\text{Tr}(\mathbf{W}^H \mathbf{S}_a \mathbf{W}) - \mathcal{P}_{d,a}) \mathbf{S}_a \mathbf{W}. \quad (28b)$$

At the current iterate $\mathbf{W}^{(t)}$, we apply the second-order Taylor expansion (also known as the Descent Lemma [26]) to construct a convex upper-bound surrogate function for $g_a (\mathbf{W})$ as

$$g_a (\mathbf{W}) \leq g_a (\mathbf{W}^{(t)}) + \text{Re}\{\text{Tr}((\mathbf{W} - \mathbf{W}^{(t)})^H \mathbf{G}_a (\mathbf{W}^{(t)}))\} + \frac{L_a^{\text{lip}}}{2} \|\mathbf{W} - \mathbf{W}^{(t)}\|_F^2 \quad (29a)$$

$$\triangleq \mathcal{U}_a (\mathbf{W} | \mathbf{W}^{(t)}), \quad (29b)$$

where L_a^{lip} is any Lipschitz constant on the Frobenius ball $\{\mathbf{W} : \|\mathbf{W}\|_F^2 \leq P_B\}$ for $\nabla g_a (\mathbf{W})$. Using matrix-norm inequalities, one obtains a choice for a global Lipschitz constant

$$L_a^{\text{lip}} = 12P_B \|\mathbf{S}_a\|_2^2 + 4\mathcal{P}_{d,a} \|\mathbf{S}_a\|_2, \quad (30)$$

with $\|\mathbf{S}_a\|_2 = \|\mathbf{f}_{S,a}\|_2$.

Proof: For any two points \mathbf{W}_1 and \mathbf{W}_2 on $g_a (\mathbf{W})$, we have

$$\begin{aligned} & \|\nabla g_a (\mathbf{W}_1) - \nabla g_a (\mathbf{W}_2)\| \\ &= 4\|(\text{Tr}(\mathbf{W}_1^H \mathbf{S}_a \mathbf{W}_1) - \mathcal{P}_{d,a}) \mathbf{S}_a (\mathbf{W}_1 - \mathbf{W}_2) \\ & \quad + (\text{Tr}(\mathbf{W}_1^H \mathbf{S}_a \mathbf{W}_1) - \text{Tr}(\mathbf{W}_2^H \mathbf{S}_a \mathbf{W}_2)) \mathbf{S}_a \mathbf{W}_2\| \quad (31a) \end{aligned}$$

$$\begin{aligned} & \leq 4\|\mathbf{S}_a\|_2 (\|\text{Tr}(\mathbf{W}_1^H \mathbf{S}_a \mathbf{W}_1) - \mathcal{P}_{d,a}\| \|\mathbf{W}_1 - \mathbf{W}_2\|_F \\ & \quad + |\text{Tr}(\mathbf{W}_1^H \mathbf{S}_a \mathbf{W}_1) - \text{Tr}(\mathbf{W}_2^H \mathbf{S}_a \mathbf{W}_2)| \|\mathbf{W}_2\|_F). \quad (31b) \end{aligned}$$

Then, according to the following inequalities for terms in (31b)

$$\begin{aligned} & |\text{Tr}(\mathbf{W}_1^H \mathbf{S}_a \mathbf{W}_1) - \text{Tr}(\mathbf{W}_2^H \mathbf{S}_a \mathbf{W}_2)| \\ &= |\text{Tr}((\mathbf{W}_1 - \mathbf{W}_2)^H \mathbf{S}_a \mathbf{W}_1) - \text{Tr}(\mathbf{W}_2^H \mathbf{S}_a (\mathbf{W}_1 - \mathbf{W}_2))| \\ &\leq \|\mathbf{W}_1 - \mathbf{W}_2\|_F \|\mathbf{S}_a\|_2 (\|\mathbf{W}_1\|_F + \|\mathbf{W}_2\|_F), \quad (32) \end{aligned}$$

$$|\text{Tr}(\mathbf{W}_1^H \mathbf{S}_a \mathbf{W}_1) - \mathcal{P}_{d,a}| \leq \|\mathbf{S}_a\|_2 \|\mathbf{W}_1\|_F^2 + \mathcal{P}_{d,a}, \quad (33)$$

$$\|\mathbf{W}_1\|_F, \|\mathbf{W}_2\|_F \leq \sqrt{P_B}, \quad (34)$$

we substitute (32)-(34) into (31) and finally obtain

$$\begin{aligned} & \|\nabla g_a (\mathbf{W}_1) - \nabla g_a (\mathbf{W}_2)\| \\ &\leq 4\|\mathbf{S}_a\|_2 (P_B \|\mathbf{S}_a\|_2 + \mathcal{P}_{d,a}) \|\mathbf{W}_1 - \mathbf{W}_2\|_F \\ & \quad + 4\|\mathbf{S}_a\|_2 (2\sqrt{P_B} \|\mathbf{S}_a\|_2 \|\mathbf{W}_1 - \mathbf{W}_2\|_F) \sqrt{P_B} \\ &= (12P_B \|\mathbf{S}_a\|_2^2 + 4\|\mathbf{S}_a\|_2 \mathcal{P}_{d,a}) \|\mathbf{W}_1 - \mathbf{W}_2\|_F, \quad (35) \end{aligned}$$

which is exactly the definition of the Lipschitz constant. \blacksquare
Consequently, replacing each $g_a (\mathbf{W})$ by its upper bound yields a concave penalization term $\rho \max\{\mathcal{U}_a (\mathbf{W} | \mathbf{W}^{(t)}) - \eta_{\text{th}}, 0\}$.

At each iteration, (29) provides a tight lower bound on $\mathbf{W}^{(t)}$ to maximize the objective function (24), guaranteeing non-decreasing penalized objective values in updates to \mathbf{W} with a standard MM step.

2) *Communication SINR term with Lagrangian dual transform (LDT) and QT for fractions:* Introducing auxiliary real-valued variables $\{\mu_k > 0, \forall k\}$, we remove the fractional term from the logarithmic function using the LDT [27]

$$\begin{aligned} & \log_2 \left(1 + \frac{|\mathbf{f}_k^H \mathbf{w}_k|^2}{\sum_{i=1, i \neq k}^{K+M} |\mathbf{f}_k^H \mathbf{w}_i|^2 + \sigma_k^2} \right) \\ &= \max_{\mu_k \geq 0} \log_2 (1 + \mu_k) - \frac{\mu_k}{\ln 2} + \frac{1 + \mu_k}{\ln 2} \frac{|\mathbf{f}_k^H \mathbf{w}_k|^2}{\sum_{i=1}^{K+M} |\mathbf{f}_k^H \mathbf{w}_i|^2 + \sigma_k^2}. \end{aligned} \quad (36)$$

Next, introducing complex-valued variables $\{y_k, \forall k\}$, we apply QT to transform the fractional SINR term into

$$\begin{aligned} & \frac{|\mathbf{f}_k^H \mathbf{w}_k|^2}{\sum_{i=1}^{K+M} |\mathbf{f}_k^H \mathbf{w}_i|^2 + \sigma_k^2} \\ &= \max_{y_k \in \mathbb{C}} 2\operatorname{Re}\{y_k^* \mathbf{f}_k^H \mathbf{w}_k\} - |y_k|^2 \left(\sum_{i=1}^{K+M} |\mathbf{f}_k^H \mathbf{w}_i|^2 + \sigma_k^2 \right). \end{aligned} \quad (37)$$

These auxiliary variables can be updated in closed form

$$\mu_k^* = \frac{|\mathbf{f}_k^H \mathbf{w}_k|^2}{\sum_{i=1, i \neq k}^{K+M} |\mathbf{f}_k^H \mathbf{w}_i|^2 + \sigma_k^2}, \quad (38)$$

$$y_k^* = \frac{\mathbf{f}_k^H \mathbf{w}_k}{\sum_{i=1}^{K+M} |\mathbf{f}_k^H \mathbf{w}_i|^2 + \sigma_k^2}. \quad (39)$$

Consequently, the communication sum rate is equivalently transformed into a non-fractional quadratic function of \mathbf{W}

$$\begin{aligned} & \mathcal{Y}(\mathbf{W} \mid \mu_k, y_k) \\ &= \frac{1 + \mu_k}{\ln 2} \left(2\operatorname{Re}\{y_k^* \mathbf{f}_k^H \mathbf{w}_k\} - |y_k|^2 \left(\sum_{i=1}^{K+M} |\mathbf{f}_k^H \mathbf{w}_i|^2 + \sigma_k^2 \right) \right). \end{aligned} \quad (40)$$

3) *Closed form solution for the QCQP:* With $\{\mu_k, y_k\}$ fixed and g_a replaced by \mathcal{U}_a , (P2) reduces to the convex quadratic constrained quadratic program (QCQP) stated as below

$$\begin{aligned} & \text{(P2.1):} \max_{\mathbf{W}} \sum_{k=1}^K \mathcal{Y}(\mathbf{W} \mid \mu_k, y_k) - \rho \max\{\mathcal{U}_a(\mathbf{W} \mid \mathbf{W}^{(t)}), 0\} \\ & \text{s.t. (22c).} \end{aligned} \quad (41)$$

In general, (P2.1) can be solved using convex optimization tools. However, we derive an efficient solution based on Lagrange duality and the Karush-Kuhn-Tucker (KKT) conditions. Specifically, if the MSE threshold is violated at the current $\mathbf{W}^{(t)}$, the objective function (41) can be compactly rewritten as a summation with a linear and a quadratic term

$$\max_{\mathbf{W}} -\operatorname{tr}(\mathbf{W}^H \mathbf{Q} \mathbf{W}) + 2\operatorname{Re}\{\operatorname{Tr}(\mathbf{P}^H \mathbf{W})\} \quad \text{s.t. (22c),} \quad (42)$$

where \mathbf{Q} and \mathbf{P} are defined by

$$\mathbf{Q} = \mathbf{Q}_C + \rho \mathbf{Q}_S, \quad (43a)$$

$$\mathbf{P} = \mathbf{P}_C + \rho \mathbf{P}_S, \quad (43b)$$

with equivalent expressions from (29) and (40) as

$$\mathbf{Q}_C = \frac{1}{\ln 2} \sum_{k=1}^K (1 + \mu_k) |y_k|^2 \mathbf{f}_k \mathbf{f}_k^H, \quad (44a)$$

$$\mathbf{Q}_S = \frac{1}{2A} \sum_{a=1}^A L_a^{\text{lip}} \mathbf{I}_{M+K}, \quad (44b)$$

$$\mathbf{P}_C = \frac{1}{\ln 2} [(1 + \mu_1) y_1 \mathbf{f}_1, \dots, (1 + \mu_K) y_K \mathbf{f}_K], \quad (44c)$$

$$\mathbf{P}_S = \frac{1}{2A} \sum_{a=1}^A \mathbf{G}_a (\mathbf{W}^{(t)}) + L_a^{\text{lip}} \mathbf{W}^{(t)}. \quad (44d)$$

The corresponding Lagrangian with a multiplier $\nu > 0$ is

$$\begin{aligned} \mathcal{L}(\mathbf{W}, \nu) &= -\operatorname{tr}(\mathbf{W}^H \mathbf{Q} \mathbf{W}) + 2\operatorname{Re}\{\operatorname{tr}(\mathbf{P}^H \mathbf{W})\} \\ &\quad - \nu (\|\mathbf{W}\|_F^2 - P_B), \end{aligned} \quad (45)$$

with KKT conditions for stationarity, complementary slackness, primal feasibility, and dual feasibility, respectively, being

$$-\mathbf{Q} \mathbf{W}^* + \mathbf{P} - \nu^* \mathbf{I} = 0, \quad (46a)$$

$$\nu^* (\|\mathbf{W}^*\|_F^2 - P_B) = 0, \quad (46b)$$

$$\|\mathbf{W}^*\|_F^2 \leq P_B, \quad (46c)$$

$$\nu^* \geq 0, \quad (46d)$$

which yields the water-filling-like solution

$$\mathbf{W}(\nu) = (\mathbf{Q} + \nu \mathbf{I})^{-1} \mathbf{P}, \quad \nu \geq 0, \quad (47)$$

where ν is found by bisection search to satisfy the power constraint (22c) with equality. Since ν enters as a scalar shift on the identity, we precompute the eigenvalue decomposition (EVD) $\mathbf{Q} = \mathbf{U} \Lambda \mathbf{U}^H$ with $\Lambda = \operatorname{diag}(\lambda_1, \dots, \lambda_M)$ and λ_m being the eigenvalue; thus, for $\nu > -\min\{\lambda_m\}_{m=1}^M$, we have

$$\mathbf{W}(\nu) = \mathbf{U} (\Lambda + \nu \mathbf{I})^{-1} \mathbf{U}^H \mathbf{P} \quad (48a)$$

$$= \mathbf{U} \operatorname{diag} \left(\left[\frac{1}{\lambda_1 + \nu}, \dots, \frac{1}{\lambda_M + \nu} \right] \right) \mathbf{U}^H \mathbf{P}, \quad (48b)$$

so each bisection step costs only a diagonal scaling, without refactorization, and evaluates

$$\|\mathbf{W}(\nu)\|_F^2 = \sum_{i=1}^M \frac{\|[\mathbf{U}^H \mathbf{P}]_{i,:}\|_2^2}{(\lambda_i + \nu)^2}, \quad (49)$$

where $[\cdot]_{i,:}$ denote the i -th row of a matrix. Furthermore, if the MSE threshold is satisfied in current $\mathbf{W}^{(t)}$, we let $\mathbf{Q} = \mathbf{Q}_C$ and $\mathbf{P} = \mathbf{P}_C$ and perform the same procedures in (43)-(49).

4) *Overall algorithm and complexity analysis for subproblem 1:* The overall low-complexity algorithm for solving (P2) is summarized in Algorithm 1. Each inner iteration performs one EVD of an $M \times M$ Hermitian matrix at cost $\mathcal{O}(M^3)$ and a scalar bisection whose per-step cost is $\mathcal{O}(M(K+M))$ to calculate $\|\mathbf{W}(\nu)\|_F^2$; the number of bisection steps grows only logarithmically with precision. The MM construction provides a tight lower bound of the penalized objective; therefore, the penalized objective in (P2) is non-decreasing over \mathbf{W} -updates. Under the power ball, the sequence $\{\mathbf{W}^{(t)}\}$ admits limit points that satisfy the first-order stationarity conditions of the surrogate built from MM and QT.

Algorithm 1 Low-complexity transmit beamforming based on QT, MM, and bisection search for (P2)

- 1: **Input:** $\{\mathbf{f}_k\}_{k=1}^K$, $\{\mathbf{f}_{S,a}\}_{a=1}^A$, $\{\mathcal{P}_{d,a}\}$, P_B , ρ , η_{th} .
- 2: **Initialization:** $\mathbf{W}^{(0)}$, using zero forcing in the first outer iterate, or using previous outer iterate results; Set $t = 0$.
- 3: **repeat**
- 4: Compute $\|S_a\|_2^2$ via (27), L_a^{lip} via (30), $\mathbf{G}_a(\mathbf{W}^{(t)})$ via (28), and $\mathcal{U}(\mathbf{W} \mid \mathbf{W}^{(t)})$ via (29).
- 5: Build $\mathbf{Q}_C, \mathbf{P}_C$ from (44); if $\mathcal{U}(\mathbf{W}^{(t)} \mid \mathbf{W}^{(t)}) > \eta_{th}$, also build $\mathbf{Q}_S, \mathbf{P}_S$, else set them to zero. Set \mathbf{Q} and \mathbf{P} via (43).
- 6: Compute EVD $\mathbf{Q} = \mathbf{U} \mathbf{A} \mathbf{U}^H$. Find ν^* by bisection using (45); set $\mathbf{W}^{(t+1)} = \mathbf{W}(\nu^*)$ via (48).
- 7: Update auxiliaries $\mu_k^{(t+1)}$ by (38) and $y_k^{(t+1)}$ by (39).
- 8: $t \leftarrow t+1$.
- 9: **until** the relative increment on the objective value of (42) or $\|\mathbf{W}^{(t)} - \mathbf{W}^{(t-1)}\|_F / \|\mathbf{W}^{(t-1)}\|_F$ below a predetermined threshold ε , or t hits the maximum number of iterations t_{\max} .
- 10: **Output:** $\mathbf{W}^* = \mathbf{W}^{(t)}$.

C. Subproblem 2: Passive Beamforming

Given fixed \mathbf{W} and $(\mathbf{r}^B, \mathbf{r}^R)$, we optimize $\boldsymbol{\theta}$ via

$$(P3) : \max_{\boldsymbol{\theta}} \sum_{k=1}^K \log_2 (1 + \text{SINR}_k(\boldsymbol{\theta})) - \rho \max \{\text{MSE}(\boldsymbol{\theta}) - \eta_{th}, 0\} \quad (50)$$

s.t. (22d).

The unique challenge in RIS passive beamforming is the unit-modulus constraint (22d). Nevertheless, it inherently defines a Riemannian manifold, known as the *complex circle manifold*

$$\mathcal{R}_{\boldsymbol{\theta}} = \{\boldsymbol{\theta} \in \mathbb{C}^N : |\theta_n| = 1, \forall n \in \mathcal{N}\}, \quad (51)$$

which enables the use of manifold optimization techniques to efficiently exploit the smoothness of objective functions and the structure of manifold feasible regions.

1) *Problem reformulation:* First, we rewrite expressions in (50) with respect to $\boldsymbol{\theta}$, and recast an unconstrained manifold optimization problem. Specifically, for the a -th angular sample, $\mathcal{P}_a(\vartheta, \varphi; \boldsymbol{\theta})$ in (18) expands as a quadratic form

$$\mathcal{P}_a(\vartheta, \varphi; \boldsymbol{\theta}) = \boldsymbol{\theta}^H \boldsymbol{\Xi}_{S,a} \boldsymbol{\theta} + 2\Re\{\boldsymbol{\xi}_{S,a}^H \boldsymbol{\theta}\} + \xi_{S,a}, \quad (52)$$

where $\boldsymbol{\Xi}_{S,a}$, $\boldsymbol{\xi}_{S,a}$, and $\xi_{S,a}$ are computed based on (14) by

$$\boldsymbol{\Xi}_{S,a} = G^R(\mathbf{r}^R) \text{diag}(\mathbf{t}_a^{\text{RT}}) \mathbf{B}^H \mathbf{W} \mathbf{W}^H \mathbf{B} \text{diag}(\mathbf{t}_a^{\text{RT}})^H, \quad (53a)$$

$$\boldsymbol{\xi}_{S,a}^H = \sqrt{G^B(\mathbf{r}^B) G^R(\mathbf{r}^R)} (\mathbf{t}_a^{\text{BT}})^H \mathbf{W} \mathbf{W}^H \mathbf{B} \text{diag}(\mathbf{t}_a^{\text{RT}}), \quad (53b)$$

$$\xi_{S,a} = G^B(\mathbf{r}^B) (\mathbf{t}_a^{\text{BT}})^H \mathbf{W} \mathbf{W}^H \mathbf{t}_a^{\text{BT}}. \quad (53c)$$

Similarly, the signal or interference term of any beam \mathbf{w}_i for the k -th communication user in the SINR expression with effective downlink channel $\mathbf{f}_k(\boldsymbol{\theta})$ can be written as

$$|\mathbf{f}_k^H(\boldsymbol{\theta}) \mathbf{w}_i|^2 = \boldsymbol{\theta}^H \boldsymbol{\Xi}_{C,k,i} \boldsymbol{\theta} + 2\Re\{\boldsymbol{\xi}_{C,k,i}^H \boldsymbol{\theta}\} + \xi_{C,k,i}, \quad (54)$$

with $\boldsymbol{\Xi}_{C,k,i}$, $\boldsymbol{\xi}_{C,k,i}$, and $\xi_{C,k,i}$ computed based on (13)

$$\boldsymbol{\Xi}_{C,k,i} = \text{diag}(\mathbf{g}_k^*) \mathbf{B}^H \mathbf{w}_i \mathbf{w}_i^H \mathbf{B} \text{diag}(\mathbf{g}_k), \quad (55a)$$

$$\boldsymbol{\xi}_{C,k,i}^H = \mathbf{h}_k^H \mathbf{w}_i \mathbf{w}_i^H \mathbf{B} \text{diag}(\mathbf{g}_k), \quad (55b)$$

$$\xi_{C,k,i} = \mathbf{h}_k^H \mathbf{w}_i \mathbf{w}_i^H \mathbf{h}_k. \quad (55c)$$

Define real-valued scalars $S_a(\boldsymbol{\theta})$, $C_{1,k}(\boldsymbol{\theta})$, and $C_{2,k}(\boldsymbol{\theta})$ as

$$S_a(\boldsymbol{\theta}) = \boldsymbol{\theta}^H \boldsymbol{\Xi}_{S,a} \boldsymbol{\theta} + 2\Re\{\boldsymbol{\xi}_{S,a}^H \boldsymbol{\theta}\} + \xi_{S,a} - \mathcal{P}_{d,a}, \quad (56a)$$

$$C_{1,k}(\boldsymbol{\theta}) = \boldsymbol{\theta}^H \boldsymbol{\Xi}_{C,k,k} \boldsymbol{\theta} + 2\Re\{\boldsymbol{\xi}_{C,k,k}^H \boldsymbol{\theta}\} + \xi_{C,k,k}, \quad (56b)$$

$$C_{2,k}(\boldsymbol{\theta}) = \sum_{i=1, i \neq k}^{K+M} \left(\boldsymbol{\theta}^H \boldsymbol{\Xi}_{C,k,i} \boldsymbol{\theta} + 2\Re\{\boldsymbol{\xi}_{C,k,i}^H \boldsymbol{\theta}\} + \xi_{C,k,i} \right) + \sigma_k^2, \quad (56c)$$

we can rewrite the objective function in (58) as

$$F(\boldsymbol{\theta}) = \sum_{k=1}^K \log_2 \left(1 + \frac{C_{1,k}(\boldsymbol{\theta})}{C_{2,k}(\boldsymbol{\theta})} \right) - \rho \max \left\{ \frac{1}{A} \sum_{a=1}^A |S_a(\boldsymbol{\theta})|^2 - \eta_{th}, 0 \right\}, \quad (57)$$

which further arrives at a standard Riemannian unconstrained manifold optimization problem stated as

$$(P3.1): \min_{\boldsymbol{\theta} \in \mathcal{R}_{\boldsymbol{\theta}}} -F(\boldsymbol{\theta}).$$

2) *RCG method:* To solve (P3.1), we adopt the Riemannian conjugate gradient (RCG) method, which generalizes the classical conjugate gradient algorithm over curved spaces, as a manifold is a topological space that locally resembles the Euclidean space [28],[29]. At any point, tangent vectors give all feasible updating directions, and their set is the tangent space

$$T_{\boldsymbol{\theta}} = \{\boldsymbol{\varsigma} \in \mathbb{C}^N : \Re\{\boldsymbol{\varsigma} \odot \boldsymbol{\theta}^*\} = \mathbf{0}\}. \quad (58)$$

Based on this definition, the RCG method proceeds by i) computing the Riemannian gradient, ii) determining the conjugate search direction, and iii) applying a retraction operation to ensure that updated variables remain on the manifold.

The Riemannian gradient is a vector field on the manifold obtained by projecting the Euclidean gradient onto the tangent space. Using Wirtinger derivatives calculus for the real-valued $F(\boldsymbol{\theta})$ with all $\boldsymbol{\Xi}_{S,a}$ and $\boldsymbol{\xi}_{C,k,i}$ being Hermitian, we obtain

$$\nabla_{\boldsymbol{\theta}} S_a(\boldsymbol{\theta}) = 2\boldsymbol{\Xi}_{S,a} \boldsymbol{\theta} + 2\boldsymbol{\xi}_{S,a}, \quad (59)$$

$$\nabla_{\boldsymbol{\theta}} C_{1,k}(\boldsymbol{\theta}) = 2\boldsymbol{\Xi}_{C,k,k} \boldsymbol{\theta} + 2\boldsymbol{\xi}_{C,k,k}, \quad (60)$$

$$\nabla_{\boldsymbol{\theta}} C_{2,k}(\boldsymbol{\theta}) = \sum_{i=1, i \neq k}^{K+M} (2\boldsymbol{\Xi}_{C,k,i} \boldsymbol{\theta} + 2\boldsymbol{\xi}_{C,k,i}). \quad (61)$$

Using the chain rule, the complete Euclidean gradient expression $\nabla_{\boldsymbol{\theta}} F(\boldsymbol{\theta})$ can be computed by (62) at the top of the next page, which is suitable for the case that the MSE threshold does not satisfy in the current $\boldsymbol{\theta}^{(j)}$; otherwise, omit the MSE-related terms in (62). Then, the Riemannian gradient is obtained via the orthogonal projection Proj for the Euclidean vector $\nabla_{\boldsymbol{\theta}} F(\boldsymbol{\theta})$ onto the tangent space $T_{\boldsymbol{\theta}}$ as follows

$$\text{Rgrad}F(\boldsymbol{\theta}) = \text{Proj}_{\boldsymbol{\theta}} (\nabla_{\boldsymbol{\theta}} F(\boldsymbol{\theta})) \quad (63a)$$

$$= \nabla_{\boldsymbol{\theta}} F(\boldsymbol{\theta}) - \text{Re}\{\nabla_{\boldsymbol{\theta}} F(\boldsymbol{\theta}) \odot \boldsymbol{\theta}^*\} \odot \boldsymbol{\theta}, \quad (63b)$$

where \odot denotes the Hadamard product. Next, in iteration j , the descent direction $\boldsymbol{\tau}^{(j)}$ for $\boldsymbol{\theta}^{(j)}$ is determined using the Polak-Ribiere formula. For brevity, the function $F(\boldsymbol{\theta}^{(j)})$ is abbreviated as $F^{(j)}$ in the following. Let $\nabla_{\mathcal{R}_{\boldsymbol{\theta}}} F^{(j)}$ denote the Riemannian gradient in iteration j . The conjugate gradient

$$\nabla_{\boldsymbol{\theta}} F(\boldsymbol{\theta}) = \frac{1}{\ln 2} \sum_{k=1}^K \frac{C_{2,k}(\boldsymbol{\theta}) \nabla_{\boldsymbol{\theta}} C_{1,k}(\boldsymbol{\theta}) - C_{1,k}(\boldsymbol{\theta}) \nabla_{\boldsymbol{\theta}} C_{2,k}(\boldsymbol{\theta})}{C_{2,k}(\boldsymbol{\theta})(C_{1,k}(\boldsymbol{\theta}) + C_{2,k}(\boldsymbol{\theta}))} - \frac{\rho}{A} \sum_{a=1}^A 2S_a(\boldsymbol{\theta}) \nabla_{\boldsymbol{\theta}} S_a(\boldsymbol{\theta}) \quad (62a)$$

$$= \frac{2}{\ln 2} \sum_{k=1}^K \frac{C_{2,k}(\boldsymbol{\Xi}_{C,k} \boldsymbol{\theta} + \boldsymbol{\xi}_{C,k}) - C_{1,k} \sum_{i=1, i \neq k}^K \boldsymbol{\Xi}_{C,k,i} \boldsymbol{\theta} + \boldsymbol{\xi}_{C,k,i}}{C_{2,k}(C_{1,k} + C_{2,k})} - \frac{4\rho}{A} \sum_{a=1}^A S_a(\boldsymbol{\theta}) (\boldsymbol{\Xi}_{S,a} \boldsymbol{\theta} + \boldsymbol{\xi}_{S,a}) \quad (62b)$$

Algorithm 2 RCG for Passive RIS Beamforming (P3)

- 1: **Input:** $\{\boldsymbol{\Xi}_{S,a}, \boldsymbol{\xi}_{S,a}, \boldsymbol{\xi}_{S,a}\}$ and $\{\boldsymbol{\Xi}_{C,k,i}, \boldsymbol{\xi}_{C,k,i}, \boldsymbol{\xi}_{C,k,i}\}$.
- 2: **Initialization:** $\boldsymbol{\theta}^{(0)}, \boldsymbol{\tau}^{(0)} = -\text{Rgrad} F(\boldsymbol{\theta}^{(0)})$.
- 3: **repeat**
- 4: Compute $\nabla_{\boldsymbol{\theta}} F(\boldsymbol{\theta}^{(j)})$ via (62) and $\text{Rgrad} F(\boldsymbol{\theta})$ via (63).
- 5: Update $\chi^{(j)}$ via (64) and search direction $\boldsymbol{\tau}^{(j)}$ via (65).
- 6: Armijo backtracking line search to get $\varpi^{(j)}$.
- 7: Perform retraction via (66) and obtain $\boldsymbol{\theta}^{(j+1)}$.
- 8: $j \leftarrow j + 1$
- 9: **until** Convergence: $\|\nabla_{\boldsymbol{\theta}} F(\boldsymbol{\theta}^{(j)})\|/\sqrt{N} \leq \varepsilon$ or $j \geq j_{\max}$.
- 10: **Output:** $\boldsymbol{\theta}^* = \boldsymbol{\theta}^{(j)}$.

update coefficient $\chi^{(j)}$, which adjusts the new search direction accounting for the curvature of the gradient, is

$$\chi^{(j)} = \frac{\langle \nabla_{\mathcal{R}_{\boldsymbol{\theta}}} F^{(j)}, \nabla_{\mathcal{R}_{\boldsymbol{\theta}}} F^{(j)} - \nabla_{\mathcal{R}_{\boldsymbol{\theta}}} F^{(j-1)} \rangle}{\langle \nabla_{\mathcal{R}_{\boldsymbol{\theta}}} F^{(j-1)}, \nabla_{\mathcal{R}_{\boldsymbol{\theta}}} F^{(j-1)} \rangle}, \quad (64)$$

where $\langle \cdot, \cdot \rangle$ denotes the Riemannian metric, being Euclidean inner product here. The descent direction is then updated as

$$\boldsymbol{\tau}^{(j)} = -\nabla_{\mathcal{R}_{\boldsymbol{\theta}}} F^{(j)} + \beta_{\boldsymbol{\theta}}^{(j)} \text{Proj}_{\boldsymbol{\theta}^{(j)}}(\boldsymbol{\tau}^{(j-1)}), \quad (65)$$

here the projection represents a simple vector transport operation. After updating the variable by moving along the descent direction, we map the new point back onto the manifold using the retraction operation, ensuing that the updated variables $\boldsymbol{\theta}^{(j+1)}$ satisfy their manifold constraints, as follows

$$\boldsymbol{\theta}^{(j+1)} = \text{Retr}_{\boldsymbol{\theta}^{(j)}}(\varpi^{(j)} \boldsymbol{\tau}^{(j)}) \quad (66a)$$

$$= \left[\frac{(\boldsymbol{\theta}^{(j)} + \varpi^{(j)} \boldsymbol{\tau}^{(j)})_n}{|(\boldsymbol{\theta}^{(j)} + \varpi^{(j)} \boldsymbol{\tau}^{(j)})_n|} \right], \quad (66b)$$

where $\varpi^{(j)}$ is the step size determined by an Armijo backtracking line search method, and the element-wise normalization ensures that $\boldsymbol{\theta}^{(j+1)}$ lies on the complex circle manifold.

3) *Overall algorithm and complexity analysis for subproblem 2:* Algorithm 2 summarizes the manifold optimization procedure, guaranteeing convergence to a stationary point under standard regularity conditions [39]. The pre-computation to build all $N \times N$ matrices $\{\boldsymbol{\Xi}_{S,a}\}_{a=1}^A$ and $\{\boldsymbol{\Xi}_{C,k,i}\}_{k \in [K], i \in [K+M]}$ scales as $\mathcal{O}(MN^2 + MN(K+M) + (A+K(K+M))N^2)$. For each RCG iteration, including objective and Riemannian gradient evaluations, line search with a constant number of trials, costs $\mathcal{O}((A+K(K+M))N^2)$, since for every grid a and pair (k, i) one performs products of the form $\boldsymbol{\Xi}_{C,k,i} \boldsymbol{\theta}$ or $\boldsymbol{\Xi}_{S,a} \boldsymbol{\theta}$ and a few additional $\mathcal{O}(N^2)$ accumulations. The total computational complexity over T_{RCG} iterations is thus $\mathcal{O}(T_{\text{RCG}}(A+K(K+M))N^2)$ plus the aforementioned precomputation. These costs can be further

reduced by avoiding explicit $N \times N$ formations and reusing the rank-1 decomposition for $\mathbf{B}^H \mathbf{W} \mathbf{W}^H \mathbf{B}$ in (53a).

D. Subproblem 3: Array Rotation Angles

Given \mathbf{W} and $\boldsymbol{\theta}$ from the previous subproblems, we jointly optimize the array rotations $(\mathbf{r}^{\text{B}}, \mathbf{r}^{\text{R}})$ of the BS and RIS via

$$\begin{aligned} (\text{P4}) : \max_{\mathbf{r}^{\text{B}}, \mathbf{r}^{\text{R}}} & \sum_{k=1}^K \log_2 (1 + \text{SINR}_k(\mathbf{r}^{\text{B}}, \mathbf{r}^{\text{R}})) \\ & - \rho \max\{\text{MSE}(\mathbf{r}^{\text{B}}, \mathbf{r}^{\text{R}}) - \eta_{\text{th}}, 0\} \end{aligned} \quad (67)$$

s.t. (22e), (22f)

Due to the highly non-concave relationships involving the cosine and exponential functions in the directivity gain and steering vectors, respectively, in the objective function, and the relatively simple box constraints on the array rotation angles, we employ the projection gradient method (PGD) [30], an effective strategy for this nonlinear maximization problem with boundary value constraints.

1) *Gradient computation:* The key step of PGD is to derive the gradient expression for the complex objective function (67). In the following, we consider the case that the rotations $(\mathbf{r}^{\text{B}}, \mathbf{r}^{\text{R}})^{(\ell)}$ in the current iteration violate the MSE threshold constraint. Thus, the MSE term is involved in the cost function; otherwise, the cost and gradient functions relate only to the communication sum rate. We adopt \mathbf{r}^{A} for any array rotation variable with $\text{A} \in \{\text{B}, \text{R}\}$ for brevity as defined in (2). Further, define a six-dimensional vector \mathbf{r} for all rotations as below

$$\mathbf{r} \triangleq [(\mathbf{r}^{\text{B}})^T, (\mathbf{r}^{\text{R}})^T]^T = [r_x^{\text{B}}, r_y^{\text{B}}, r_z^{\text{B}}, r_x^{\text{R}}, r_y^{\text{R}}, r_z^{\text{R}}]^T \in \mathbb{R}^6. \quad (68)$$

The gradient of (67) w.r.t. the generic rotation vector \mathbf{r} is

$$\begin{aligned} \frac{\partial F(\mathbf{r})}{\partial \mathbf{r}} = & -\frac{2\rho}{A} \sum_{a=1}^A (\mathcal{P}_a(\mathbf{r}) - \mathcal{P}_{\text{d},a}) \frac{\partial \mathcal{P}_a(\mathbf{r})}{\partial \mathbf{r}} \\ & + \frac{1}{\ln 2} \sum_{k=1}^K \frac{1}{1 + \text{SINR}_k(\mathbf{r})} \frac{\partial \text{SINR}_k(\mathbf{r})}{\partial \mathbf{r}}, \end{aligned} \quad (69)$$

where $\frac{\partial \text{SINR}_k(\mathbf{r})}{\partial \mathbf{r}}$ and $\frac{\partial \mathcal{P}_a(\mathbf{r})}{\partial \mathbf{r}}$ are the two main computational branches.

Define the signal and interference terms in the SINR expression by $C_{1,k}(\mathbf{r}) = |\mathbf{f}_k^H(\mathbf{r}) \mathbf{w}_k|^2$ and $C_{2,k}(\mathbf{r}) = \sum_{i \neq k} |\mathbf{f}_k^H(\mathbf{r}) \mathbf{w}_i|^2 + \sigma_k^2$, respectively. Then we have

$$\frac{\partial \text{SINR}_k(\mathbf{r})}{\partial \mathbf{r}} = \frac{\frac{\partial C_{1,k}(\mathbf{r})}{\partial \mathbf{r}} C_{2,k}(\mathbf{r}) - C_{1,k}(\mathbf{r}) \frac{\partial C_{2,k}(\mathbf{r})}{\partial \mathbf{r}}}{(C_{2,k}(\mathbf{r}))^2}, \quad (70)$$

with

$$\frac{\partial C_{1,k}(\mathbf{r})}{\partial \mathbf{r}} = 2\operatorname{Re}\left\{\left(\frac{\partial \mathbf{f}_k(\mathbf{r})}{\partial \mathbf{r}}\right)^H \mathbf{w}_k \mathbf{w}_k^H \mathbf{f}_k(\mathbf{r})\right\}, \quad (71a)$$

$$\frac{\partial C_{2,k}(\mathbf{r})}{\partial \mathbf{r}} = \sum_{i \neq k} 2\operatorname{Re}\left\{\left(\frac{\partial \mathbf{f}_k(\mathbf{r})}{\partial \mathbf{r}}\right)^H \mathbf{w}_i \mathbf{w}_i^H \mathbf{f}_k(\mathbf{r})\right\}. \quad (71b)$$

According to the effective user channel (13), we derive

$$\frac{\partial \mathbf{f}_k(\mathbf{r})}{\partial \mathbf{r}^B} = \frac{\partial \mathbf{h}_k(\mathbf{r}^B)}{\partial \mathbf{r}^B} + \frac{\partial \mathbf{B}(\mathbf{r})}{\partial \mathbf{r}^B} \operatorname{diag}(\boldsymbol{\theta}) \mathbf{g}_k(\mathbf{r}^R), \quad (72a)$$

$$\frac{\partial \mathbf{f}_k(\mathbf{r})}{\partial \mathbf{r}^R} = \frac{\partial \mathbf{B}(\mathbf{r})}{\partial \mathbf{r}^R} \operatorname{diag}(\boldsymbol{\theta}) \mathbf{g}_k(\mathbf{r}^R) + \mathbf{B}(\mathbf{r}) \operatorname{diag}(\boldsymbol{\theta}) \frac{\partial \mathbf{g}_k(\mathbf{r}^R)}{\partial \mathbf{r}^R}, \quad (72b)$$

where $\frac{\partial \mathbf{h}_k(\mathbf{r}^B)}{\partial \mathbf{r}^B}$, $\frac{\partial \mathbf{g}_k(\mathbf{r}^R)}{\partial \mathbf{r}^R}$, $\frac{\partial \mathbf{B}(\mathbf{r})}{\partial \mathbf{r}^R}$, and $\frac{\partial \mathbf{B}(\mathbf{r})}{\partial \mathbf{r}^B}$ can be computed in (88) at the top of the next page.

Then we compute the derivatives of the steering vectors. We denote $\mathbf{X} \in \{\text{BT, RT, BR, RB, BU, RU}\}$, and omit the index for all the steering vectors with the same element-wise structure. For a generic steering vector,

$$\mathbf{t}^X(\mathbf{r}^A) \triangleq [e^{j\frac{2\pi}{\lambda}(\mathbf{u}^X)^T \mathbf{d}_1^A(\mathbf{r}^A)}, \dots, e^{j\frac{2\pi}{\lambda}(\mathbf{u}^X)^T \mathbf{d}_J^A(\mathbf{r}^A)}]^T, \quad (73)$$

with element positions $\mathbf{d}_v^A(\mathbf{r}^A) = \mathbf{d}_0^A + \mathbf{R}(\mathbf{r}^A) \bar{\mathbf{d}}_v^A$ as depicted in (4) and $v \in \{m, n\}$ denoting the index of BS or RIS element, the following relationships hold based on chain rules

$$\frac{\partial \mathbf{t}^X(\mathbf{r}^A)}{\partial \mathbf{r}^A} = \operatorname{diag}(\boldsymbol{\omega}^X(\mathbf{r}^A)) \mathbf{t}^X(\mathbf{r}^A), \quad (74a)$$

$$\omega_v^X(\mathbf{r}^A) = j \frac{2\pi}{\lambda} (\mathbf{u}^X)^T \frac{\partial \mathbf{d}_v^A(\mathbf{r}^A)}{\partial \mathbf{r}^A}, \quad (74b)$$

$$\frac{\partial \mathbf{d}_v^A(\mathbf{r}^A)}{\partial \mathbf{r}^A} = \left[\frac{\partial \mathbf{R}(\mathbf{r}^A)}{\partial r_x^A} \bar{\mathbf{d}}_v^A, \frac{\partial \mathbf{R}(\mathbf{r}^A)}{\partial r_y^A} \bar{\mathbf{d}}_v^A, \frac{\partial \mathbf{R}(\mathbf{r}^A)}{\partial r_z^A} \bar{\mathbf{d}}_v^A \right]. \quad (74c)$$

The derivatives of the rotation matrix $\mathbf{R}(\mathbf{r}^A) = \mathbf{R}_x(r_x^A) \mathbf{R}_y(r_y^A) \mathbf{R}_z(r_z^A)$ w.r.t each rotation variable are

$$\frac{\partial \mathbf{R}(\mathbf{r}^A)}{\partial r_x^A} = \frac{\partial \mathbf{R}_x(r_x^A)}{\partial r_x^A} \mathbf{R}_y(r_y^A) \mathbf{R}_z(r_z^A), \quad (75a)$$

$$\frac{\partial \mathbf{R}(\mathbf{r}^A)}{\partial r_y^A} = \mathbf{R}_x(r_x^A) \frac{\partial \mathbf{R}_y(r_y^A)}{\partial r_y^A} \mathbf{R}_z(r_z^A), \quad (75b)$$

$$\frac{\partial \mathbf{R}(\mathbf{r}^A)}{\partial r_z^A} = \mathbf{R}_x(r_x^A) \mathbf{R}_y(r_y^A) \frac{\partial \mathbf{R}_z(r_z^A)}{\partial r_z^A}, \quad (75c)$$

and according to the definition in (3), we have

$$\frac{\partial \mathbf{R}_x(r_x^A)}{\partial r_x^A} = \begin{bmatrix} 0 & 0 & 0 \\ 0 & -\sin r_x^A & -\cos r_x^A \\ 0 & \cos r_x^A & -\sin r_x^A \end{bmatrix}, \quad (76a)$$

$$\frac{\partial \mathbf{R}_y(r_y^A)}{\partial r_y^A} = \begin{bmatrix} -\sin r_y^A & 0 & \cos r_y^A \\ 0 & 0 & 0 \\ -\cos r_y^A & 0 & -\sin r_y^A \end{bmatrix}, \quad (76b)$$

$$\frac{\partial \mathbf{R}_z(r_z^A)}{\partial r_z^A} = \begin{bmatrix} -\sin r_z^A & -\cos r_z^A & 0 \\ \cos r_z^A & -\sin r_z^A & 0 \\ 0 & 0 & 0 \end{bmatrix}. \quad (76c)$$

For the directional gains and their derivatives, let $\bar{\mathbf{n}} = [0, 0, 1]^T$ and $\mathbf{n}(\mathbf{r}^A) = \mathbf{R}(\mathbf{r}^A) \bar{\mathbf{n}}$ be the array boresight. According to the practical directivity model (11), we have

$$\frac{\partial \sqrt{G}}{\partial \mathbf{r}} = \frac{1}{2\sqrt{G}} \frac{\partial G}{\partial \mathbf{r}}. \quad (77a)$$

$$\frac{\partial G^A}{\partial \mathbf{r}^A} = G_0^A p^A (-\mathbf{n}^T \mathbf{u})^{p^A-1} \left(-\frac{\partial \mathbf{n}^T}{\partial \mathbf{r}^A} \mathbf{u} \right), \quad (77b)$$

$$\frac{\partial \mathbf{n}^T}{\partial \mathbf{r}^A} = \bar{\mathbf{n}}^T \frac{\partial \mathbf{R}(\mathbf{r}^A)}{\partial \mathbf{r}^A}. \quad (77c)$$

At the non-differentiable boundary, subgradients are used.

According to the sensing beam pattern (18) and the sensing channel model (14), for the beam-pattern derivative,

$$\frac{\partial \mathcal{P}_a}{\partial \mathbf{r}^A} = 2\Re\left\{\left(\frac{\partial \mathbf{f}_{S,a}(\mathbf{r})}{\partial \mathbf{r}^A}\right)^H \mathbf{W} \mathbf{W}^H \mathbf{f}_{S,a}(\mathbf{r})\right\}, \quad (79)$$

where $\frac{\partial \mathbf{f}_{S,a}(\mathbf{r})}{\partial \mathbf{r}^A}$ is computed in (80). It is also convenient to gather partials into Jacobians $\mathbf{J}_{S,a}^{(A)} \triangleq \left[\frac{\partial \mathbf{f}_{S,a}}{\partial r_x^A}, \frac{\partial \mathbf{f}_{S,a}}{\partial r_y^A}, \frac{\partial \mathbf{f}_{S,a}}{\partial r_z^A} \right] \in \mathbb{C}^{N_t \times 3}$ similar to (74), so that (79) compacts to

$$\frac{\partial \mathcal{P}_a}{\partial \mathbf{r}^A} = 2\Re\left\{\mathbf{J}_{S,a}^{(A)H} \mathbf{W} \mathbf{W}^H \mathbf{f}_{S,a}\right\} \in \mathbb{R}^3. \quad (81)$$

2) *Projected-gradient framework for the rotation block.*: Let $\mathcal{D} \triangleq \mathcal{D}_B \times \mathcal{D}_R$ be the box of angle limits in (P4) with

$$\mathcal{D}_A = \{\mathbf{r}^A : \mathbf{r}_{lb}^A \leq \mathbf{r}^A \leq \mathbf{r}_{ub}^A\}, \quad (82)$$

and denote $\mathbf{r}_{lb} \triangleq [(\mathbf{r}_{lb}^B)^T, (\mathbf{r}_{lb}^R)^T]^T$, and $\mathbf{r}_{ub} \triangleq [(\mathbf{r}_{ub}^B)^T, (\mathbf{r}_{ub}^R)^T]^T$. Let $\Pi_{\mathcal{D}}(\cdot)$ be the Euclidean projection onto \mathcal{D} . We perform projected gradient ascent on F with the projected step

$$\boldsymbol{\beta}(\alpha) = \Pi_{\mathcal{D}}(\mathbf{r} + \alpha \nabla_{\mathbf{r}} F(\mathbf{r})) - \mathbf{r}, \quad (83)$$

for any step size $\alpha > 0$. Define the projected-gradient mapping $\mathbf{H}_{\alpha}(\mathbf{r}) \triangleq \frac{1}{\alpha} \boldsymbol{\beta}(\alpha)$, for any $\alpha > 0$, \mathbf{r}^* is a first-order stationary point of (P4) if and only if $\mathbf{H}_{\alpha}(\mathbf{r}^*) = \mathbf{0}$, according to the KKT condition. Hence $\|\mathbf{H}_{\alpha}(\mathbf{r})\|_2$ is a valid criticality measure for stopping. Because \mathcal{D} is a box, the projection (83) reduces to the componentwise clipping

$$\boldsymbol{\beta}^{(\ell)}(\alpha) = \operatorname{clip}(\mathbf{r}^{(\ell)} + \alpha \nabla_{\mathbf{r}} F^{(\ell)}(\mathbf{r}))_{[\mathbf{r}_{lb}, \mathbf{r}_{ub}]} - \mathbf{r}^{(\ell)}, \quad (84)$$

where the clip $\operatorname{clip}(x)_{[y,z]} = \min\{\max\{x, y\}, z\}$ acts elementwise. Given the previous $(\mathbf{r}, F(\mathbf{r}), \nabla F(\mathbf{r}))^{(\ell-1)}$, the stepsize uses Barzilai–Borwein initialization

$$\alpha_{BB} = \frac{\|\mathbf{r}^{(\ell)} - \mathbf{r}^{(\ell-1)}\|^2}{(\mathbf{r}^{(\ell)} - \mathbf{r}^{(\ell-1)})^T (\nabla F(\mathbf{r}^{(\ell)}) - \nabla F(\mathbf{r}^{(\ell-1)}))}, \quad (85)$$

and clip to $[\alpha_{\min}, \alpha_{\max}]$ to ensure robustness. An Armijo backtracking is then performed until the ascent rule holds

$$F(\mathbf{r} + \boldsymbol{\beta}(\alpha)) \geq F(\mathbf{r}) + c_1 \nabla_{\mathbf{r}} F(\mathbf{r})^T \boldsymbol{\beta}(\alpha), \quad (86)$$

with $c_1 \in (0, 1)$ and the backtracking using $\alpha \leftarrow c_2 \alpha$, $c_2 \in (0, 1)$. The iteration terminates when it meets the stopping criteria that the projected gradient norm is small, i.e., $\|\mathbf{H}_{\alpha}(\mathbf{r}^{(\ell)})\|_2 \leq \varepsilon_{pg}$, or the relative step is small, i.e., $\frac{\|\mathbf{r}^{(\ell)} - \mathbf{r}^{(\ell-1)}\|_2}{\max\{1, \|\mathbf{r}^{(\ell-1)}\|_2\}} \leq \varepsilon_{rel}$. For box constraints, $\mathbf{H}_{\alpha}(\mathbf{r}^{(\ell)})$ admits

$$\frac{\partial \mathbf{h}_k(\mathbf{r}^B)}{\partial \mathbf{r}^B} = \sum_{l=1}^{L_k} a_{k,l} \left[\frac{\partial \sqrt{G_{k,l}^B(\mathbf{r}^B)}}{\partial \mathbf{r}^B} \mathbf{t}_{k,l}^{\text{BU}}(\mathbf{r}^B) + \sqrt{G_{k,l}^B(\mathbf{r}^B)} \frac{\partial \mathbf{t}_{k,l}^{\text{BU}}(\mathbf{r}^B)}{\partial \mathbf{r}^B} \right] \quad (78\text{a})$$

$$\frac{\partial \mathbf{g}_k(\mathbf{r}^R)}{\partial \mathbf{r}^R} = \sum_{q=1}^{Q_k} c_{k,q} \left[\frac{\partial \sqrt{G_{k,q}^R(\mathbf{r}^R)}}{\partial \mathbf{r}^R} \mathbf{t}_{k,q}^{\text{RU}}(\mathbf{r}^R) + \sqrt{G_{k,q}^R(\mathbf{r}^R)} \frac{\partial \mathbf{t}_{k,q}^{\text{RU}}(\mathbf{r}^R)}{\partial \mathbf{r}^R} \right]. \quad (78\text{b})$$

$$\frac{\partial \mathbf{B}(\mathbf{r})}{\partial \mathbf{r}^B} = \sum_{p=1}^P b_p \left[\frac{\partial \sqrt{G_{k,p}^B(\mathbf{r}^B)}}{\partial \mathbf{r}^B} \sqrt{G_{k,p}^R(\mathbf{r}^R)} \mathbf{t}_p^{\text{BR}}(\mathbf{r}^B) (\mathbf{t}_p^{\text{RB}}(\mathbf{r}^R))^H + \sqrt{G_{k,p}^B(\mathbf{r}^B)} G_{k,p}^R(\mathbf{r}^R) \frac{\partial \mathbf{t}_p^{\text{BR}}(\mathbf{r}^B)}{\partial \mathbf{r}^B} (\mathbf{t}_p^{\text{RB}}(\mathbf{r}^R))^H \right], \quad (78\text{c})$$

$$\frac{\partial \mathbf{B}(\mathbf{r})}{\partial \mathbf{r}^R} = \sum_{p=1}^P b_p \left[\sqrt{G_{k,p}^B(\mathbf{r}^B)} \frac{\partial \sqrt{G_{k,p}^R(\mathbf{r}^R)}}{\partial \mathbf{r}^R} \mathbf{t}_p^{\text{BR}}(\mathbf{r}^B(\mathbf{r}^B)) (\mathbf{t}_p^{\text{RB}}(\mathbf{r}^R))^H + \sqrt{G_{k,p}^B(\mathbf{r}^B)} G_{k,p}^R(\mathbf{r}^R) \mathbf{t}_p^{\text{BR}}(\mathbf{r}^B) \left(\frac{\partial \mathbf{t}_p^{\text{RB}}(\mathbf{r}^R)}{\partial \mathbf{r}^R} \right)^H \right], \quad (78\text{d})$$

$$\frac{\partial \mathbf{f}_{S,a}(\mathbf{r}^B, \mathbf{r}^R)}{\partial \mathbf{r}^B} = a_a \frac{\partial \left(\sqrt{G_a^B(\mathbf{r}^B)} \mathbf{t}^{\text{BT}}(\mathbf{r}^B) \right)}{\partial \mathbf{r}^B} + c_a \frac{\partial \mathbf{B}(\mathbf{r}^B, \mathbf{r}^R)}{\partial \mathbf{r}^B} \text{diag}(\boldsymbol{\theta}) \sqrt{G_a^R(\mathbf{r}^R)} \mathbf{t}^{\text{RT}}(\mathbf{r}^R), \quad (80\text{a})$$

$$\frac{\partial \mathbf{f}_{S,a}(\mathbf{r}^B, \mathbf{r}^R)}{\partial \mathbf{r}^R} = a_a \frac{\partial \mathbf{B}(\mathbf{r}^B, \mathbf{r}^R)}{\partial \mathbf{r}^R} \text{diag}(\boldsymbol{\theta}) \sqrt{G_a^R(\mathbf{r}^R)} \mathbf{t}^{\text{RT}} + c_a \mathbf{B}(\mathbf{r}^B, \mathbf{r}^R) \text{diag}(\boldsymbol{\theta}) \frac{\partial \left(\sqrt{G_a^R(\mathbf{r}^R)} \mathbf{t}^{\text{RT}}(\mathbf{r}^R) \right)}{\partial \mathbf{r}^R} \quad (80\text{b})$$

Algorithm 3 PGD for Array Rotation Subproblem (P4)

- 1: **Input:** fixed $(\mathbf{W}, \boldsymbol{\theta})$, box \mathcal{D} , tolerances $\varepsilon_{\text{pg}}, \varepsilon_{\text{rel}} > 0$, and maximum iterations $I_{\text{PGD}}^{\text{max}}$.
- 2: **Initialization:** initial point $\mathbf{r}^{(0)} \in \mathcal{D}$
- 3: **for** $\ell = 0, 1, \dots, I_{\text{PGD}}^{\text{max}} - 1$ **do**
- 4: Evaluate the cost $F(\mathbf{r}^{(\ell)})$ and the gradient $\nabla_{\mathbf{r}} F(\mathbf{r}^{(\ell)})$ using (67)-(81).
- 5: **if** $\ell > 0$ **then**
- 6: Barzilai-Borwein stepsize initialization $\alpha^{(\ell)} \leftarrow \alpha_{\text{BB}}$ via (85).
- 7: **else**
- 8: $\alpha^{(\ell)} \leftarrow \alpha_0$.
- 9: **end if**
- 10: Find stepsize $\alpha^{(\ell)}$ via Armijo backtracking to satisfy (86).
- 11: Determine projected step $\boldsymbol{\beta}^{(\ell)}(\alpha)$ via (84)
- 12: Update optimization variables by $\mathbf{r}^{(\ell+1)} = \mathbf{r}^{(\ell)} + \boldsymbol{\beta}^{(\ell)}(\alpha)$.
- 13: Compute projected gradient mapping $\mathbf{H}_{\alpha}(\mathbf{r}^{(\ell)})$ via (87).
- 14: **if** $\|\mathbf{H}_{\alpha}(\mathbf{r}^{(\ell+1)})\|_2 \leq \varepsilon_{\text{pg}}$ **or** $\frac{\|\mathbf{r}^{(\ell+1)} - \mathbf{r}^{(\ell)}\|_2}{\max\{1, \|\mathbf{r}^{(\ell)}\|_2\}} \leq \varepsilon_{\text{rel}}$ **then**
- 15: **break**;
- 16: **end if**
- 17: **end for**
- 18: **Output:** $\mathbf{r}^B \leftarrow \mathbf{r}_{1:3}^{(\ell+1)}, \mathbf{r}^R \leftarrow \mathbf{r}_{4:6}^{(\ell+1)}$.

the following componentwise form for i -th entry independent of α

$$[\mathbf{H}_{\alpha}(\mathbf{r}^{(\ell)})]_i = \begin{cases} [\nabla_{\mathbf{r}} F^{(\ell)}(\mathbf{r})]_i, & r_{\text{lb},i} < r_i < r_{\text{ub},i} \\ \max\{0, [\nabla_{\mathbf{r}} F^{(\ell)}(\mathbf{r})]_i\}, & r_i = r_{\text{lb},i}, \\ \min\{0, [\nabla_{\mathbf{r}} F^{(\ell)}(\mathbf{r})]_i\}, & r_i = r_{\text{ub},i}. \end{cases} \quad (87)$$

The gradient cost is dominated by Jacobians (80) of rotation-related steering vectors and derivatives (78) with matrix-chain products. Because the directional-gain model is piecewise smooth, we use subgradients at the visibility boundary and a smooth gating for stable line search.

3) *Overall algorithm under penalty-based AO framework for original problem 1:* Algorithm 4 summarizes the overall projected gradient method. For the per-iteration computational complexity, directly forming \mathbf{B} and the Jacobians as dense

$M \times N$ matrices yields $\mathcal{O}(PMN)$ computations per rotation axis, and evaluating the sensing gradients over A grids would add $\mathcal{O}(AMN)$. However, using the rank- P factorization for \mathbf{B} and its derivatives, all costly matrix–vector products, involving \mathbf{B} and $\partial \mathbf{B} / \partial r_i^A$, are computed without materializing $M \times N$ blocks and costing $\mathcal{O}(NP)$ plus $\mathcal{O}(MP)$. With these reuses, one PGD iteration with full gradient of F has the leading cost: i) precomputation on steering vectors and their Jacobians with $\mathcal{O}(P(M+N))$, ii) sensing and communication channel–Jacobian products $\mathcal{O}((A+K)P(N+M))$, iii) use $\mathbf{W}(\mathbf{W}^H \mathbf{f})$ to apply $\mathbf{W}\mathbf{W}^H$ in (71) and (81) with $\mathcal{O}((M+K)M(A+K))$. Therefore, the per-iteration complexity scales as $\mathcal{O}(P(M+N)(A+K+1) + (M+K)M(A+K))$ with a constant coefficient affected by backtracking searches.

E. Overall algorithm

Finally, we adopt a penalty-assisted AO-based algorithm framework over $(\mathbf{W}, \boldsymbol{\theta}, \mathbf{r}^B, \mathbf{r}^R)$, resulting in an overall algorithm with nested loops summarized in Algorithm 4, where we obtain a suboptimal solution for the original problem (P1). At the δ -th outer iteration, with the other blocks fixed, we first solve (P2) by Algorithm 1 to update $\mathbf{W}^{(\delta+1)}$; next solve (P3) by Algorithm 2 to update $\boldsymbol{\theta}^{(\delta+1)}$; then solve (P4) by Algorithm 3 (projected-gradient over the box \mathcal{D}) to obtain $(\mathbf{r}^B, \mathbf{r}^R)^{(\delta+1)}$. After the three inner loops, the penalty weight is refreshed as $\rho^{(\delta+1)} \leftarrow \gamma_{\rho} \rho^{(\delta)}$ if the MSE constraint is violated (i.e., $\text{MSE} > \eta_{\text{th}}$); otherwise $\rho^{(\delta+1)} = \rho^{(\delta)}$. Each inner solver uses its own line search/tolerances to guarantee ascent of the penalized objective and is warm-started from the previous iterate. The outer loop terminates when the fractional increase of the penalized objective in (P1.1) falls below ε_{AO} and the MSE constraint is satisfied ($\text{MSE} \leq \eta_{\text{th}}$).

IV. SIMULATION RESULTS

This section presents numerical results for the proposed rotatable BS–RIS ISAC design. Unless otherwise stated, the

Algorithm 4 Penalty-assisted AO-based Algorithm for (P1)

```

1: Input:  $\mathbf{u}_{k,l}^{\text{BU}}, \mathbf{u}_p^{\text{RB}}, \mathbf{u}_p^{\text{BR}}, \mathbf{u}_{k,q}^{\text{RU}}, \mathbf{u}_a^{\text{BT}}, \mathbf{u}_a^{\text{RT}}, \gamma_\rho > 0$ , and  $\mathcal{P}_d(\vartheta_a, \varphi_a)$ .
2: Initialization:  $\mathbf{W}^{(0)}, \boldsymbol{\theta}^{(0)}, (\mathbf{r}^A, \mathbf{r}^B)^{(0)}, \rho^{(0)}$  and  $\delta = 0$ 
3: repeat
4:   Solve subproblem (P2) via Algorithm 1 to obtain  $\mathbf{W}^{(\delta+1)}$ .
5:   Solve subproblem (P3) via Algorithm 2 to obtain  $\boldsymbol{\theta}^{(\delta+1)}$ .
6:   Solve subproblem (P4) via Algorithm 3 to obtain  $(\mathbf{r}^A, \mathbf{r}^B)^{(\delta+1)}$ .
7:   if Current MSE value violates the threshold  $\eta_{\text{th}}$  then
8:      $\rho^{(\delta+1)} = \gamma \rho^{(\delta)}$ .
9:   else
10:     $\rho^{(\delta+1)} = \rho^{(\delta)}$ .
11:   end if
12:    $\delta \leftarrow \delta + 1$ .
13: until the fractional increase of the objective value of problem (P1.1) is smaller than a threshold  $\varepsilon_{\text{AO}}$  and the MSE is below the threshold  $\eta_{\text{th}}$ .
14: Output:  $\mathbf{W} \leftarrow \mathbf{W}^{(\delta)}, \boldsymbol{\theta} \leftarrow \boldsymbol{\theta}^{(\delta)}, \mathbf{r}^A \leftarrow \mathbf{r}^{A,(\delta)}, \mathbf{r}^B \leftarrow \mathbf{r}^{B,(\delta)}$ .

```

BS is equipped with a $M = M_x M_y = 2 \times 2$ antennas by default with inter-element spacing $d_x = d_y = \lambda/2$ for a carrier wavelength $\lambda = 0.1$ m. The RIS is modeled as a 6×6 UPA with spacing $e_x = e_y = \lambda/2$, located at $(10, 0, 0)$ m relative to the BS. The unrotated BS and RIS boresights are aligned with the positive z -axis, and their orientations are parameterized by rotation vectors \mathbf{r}^B and \mathbf{r}^R . The small-scale fading of all links follows a geometry-based multipath model: each BS–user and RIS–user channel comprises $L_k = Q_k = 2$ paths with independently generated azimuth and elevation angles, uniformly distributed over $[-\pi, \pi]$ and $[-\pi/3, \pi/3]$, respectively, and complex Gaussian path gains with normalized variance. The cascaded BS–RIS channel contains $P = 2$ paths with angles and gains drawn independently. Thermal noise at each user is modeled as circularly symmetric complex Gaussian with variance $\sigma_k^2 = 10^{-6}$. For sensing, the BS forms a monostatic beampattern over a two-dimensional angular grid with $A_{\text{az}} = 11$ azimuth and $A_{\text{el}} = 6$ elevation samples, uniformly spanning $\phi \in [-\pi, \pi]$ and $\vartheta \in [-\pi/4, \pi/4]$. The desired sensing pattern corresponds to two spotlight-like angular sectors, and the target threshold of sensing MSE is $\eta_{\text{th}} = 0.2$. The total BS transmit power is $P_B = 30$ dBm.

We adopt both half-space isotropic and directional element patterns. In the directional case, the BS and RIS element gains follow the piecewise model (11), while $G_{0,B} = G_{0,R} = 2$ are constant in the isotropic case. For each random channel realization, the proposed alternating optimization algorithm jointly updates the BS precoder \mathbf{W} , the RIS phase vector $\boldsymbol{\theta}$, and the rotations $(\mathbf{r}^B, \mathbf{r}^R)$ so as to maximize the downlink sum rate $\sum_{k=1}^K \log_2(1 + \text{SINR}_k)$ under the sensing MSE constraint. To assess the gain of spatial geometry control and RIS assistance, we compare the fully rotatable BS–RIS architecture (“Rot-BS+Rot-RIS”) with four benchmarks: (i) only the BS is rotatable while the RIS orientation is fixed (“Rot-BS+Fix-RIS”); (ii) only the RIS is rotatable (“Fix-BS+Rot-RIS”); (iii) both BS and RIS are fixed (“Fix-BS+Fix-RIS”); and two non-RIS baseline (iv) (“Rot-BS+No-RIS”) and (v) (“Fix-BS+No-RIS”), where the RIS–user link is disabled by setting the RIS–user path gains to zero. All reported curves are obtained by averaging the communication and sensing metrics over a large number of independent channel realizations.

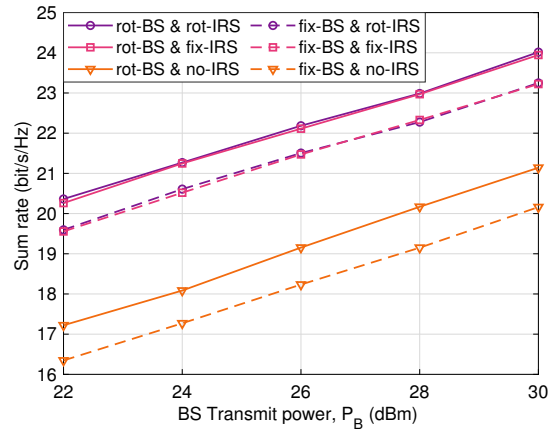


Fig. 2. Sum rate versus maximum transmit power under $p^R = p^B = 0$ with $N = 6 \times 6$, $M = 2 \times 2$ and $K = 2$.

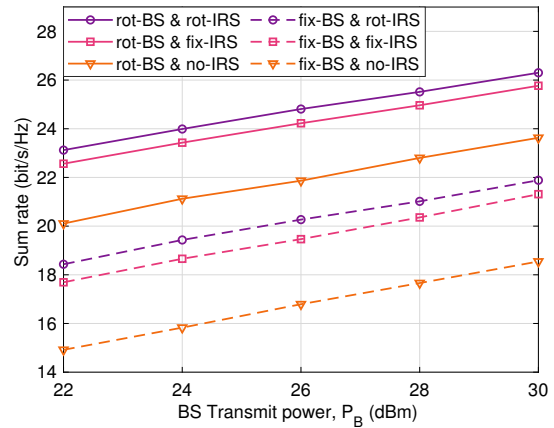


Fig. 3. Sum rate versus maximum transmit power under $p^R = p^B = 2$ with $N = 6 \times 6$, $M = 2 \times 2$ and $K = 2$.

Figs. 2 and 3 illustrate the sum rate versus the BS transmit power under the sensing beampattern MSE constraint for a 2×2 transmit array, two communication users, and two sensing directions. In the half-space isotropic case (Fig. 2), all schemes benefit from increasing power, showing roughly linear growth at low-to-moderate SNR and gradual saturation when multiuser interference and the sensing constraint become dominant. Across the entire power range, the proposed joint BS–RIS rotation (“Rot-BS+Rot-RIS”) consistently achieves the highest sum rate, followed by the partially rotatable schemes. At the same time, the non-RIS baselines perform worse due to their reduced effective aperture. However, the RIS array rotations seem not to be effective in the half-space isotropic case, because rotations in this case cannot reap the directivity gains; one can say that isotropic elements avoid severe signal degradation in side-lobe directions. With a directional half-space pattern (Fig. 3, element directivity factor 2), all curves shift upward, confirming the SNR and throughput gains brought by element directivity. At the same time, the rate gap between Rot-BS+Rot-RIS and the benchmark schemes becomes more pronounced, as the proposed design better aligns the main lobes with user directions and steers reduced-gain regions toward the sensing directions, thereby alleviating the performance penalty of the sensing constraint. This indicates that geometric adaptation, especially when both

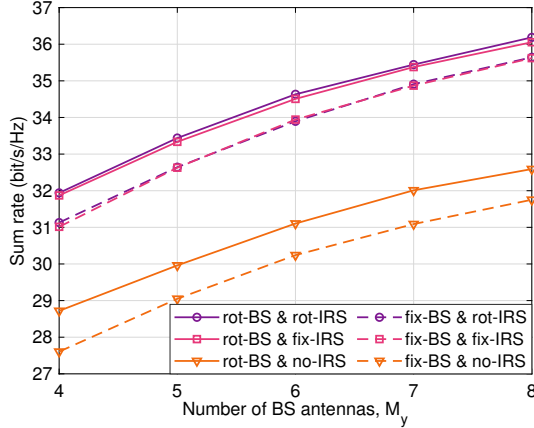


Fig. 4. Sum rate versus the number of BS antennas under $p^R = p^B = 0$ with $N = 6 \times 6$, $M_x = 1$ $P = 30$ dBm, and $K = 3$.

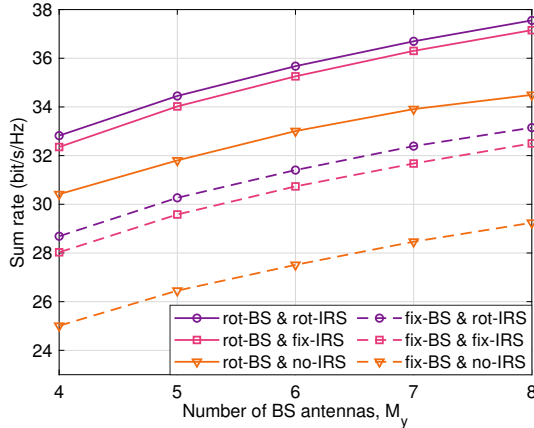


Fig. 5. Sum rate versus the number of BS antennas under $p^R = p^B = 2$ with $N = 6 \times 6$, $M_x = 1$ $P = 30$ dBm, and $K = 3$.

active and passive arrays are rotatable, becomes increasingly valuable in the interference-limited regime and practical BS antenna or RIS element radiation patterns.

Figs. 4 and 5 examine the impact of the number of transmit antennas for a $1 \times M_y$ BS array with three users. In the isotropic case (Fig. 4), the sum rate of all schemes increases with M_y , since a larger array aperture provides stronger array gain and finer spatial resolution to separate the three users while shaping the sensing beampattern. Schemes with only BS rotation or only RIS rotation still benefit from adding antennas, but their curves remain noticeably below the fully rotatable configuration, indicating that partial geometric adaptation cannot fully unlock the potential of a large array in the presence of both multiuser interference and sensing requirements. The non-RIS baselines lie at the bottom in all M_y , highlighting the importance of the extra reflecting aperture with more spatial resources. In the directional case (Fig. 5), all curves are further elevated and the advantage of Rot-BS+Rot-RIS becomes more marked. The directivity amplifies the relative advantage of the joint BS-RIS rotation: by aligning the main lobe of the transmit array and the dominant reflecting directions of the RIS with the user angles while steering reduced-gain regions toward the sensing directions, the proposed design can more efficiently decouple communication beams from sensing beams, leading to a larger rate gain over the partially rotatable

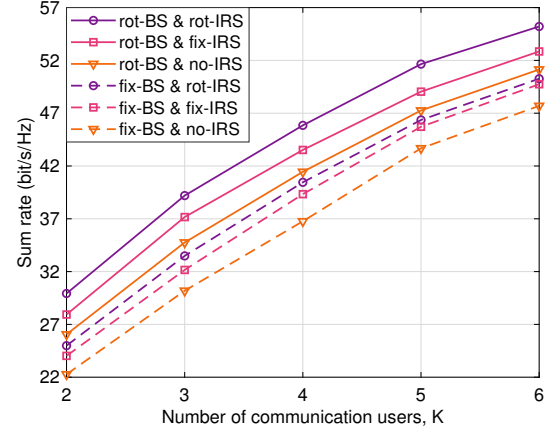


Fig. 6. Sum rate versus the number of communication users under $p^R = p^B = 2$ with $N = 6 \times 6$, $M = 2 \times 4$, and $P = 22$ dBm.

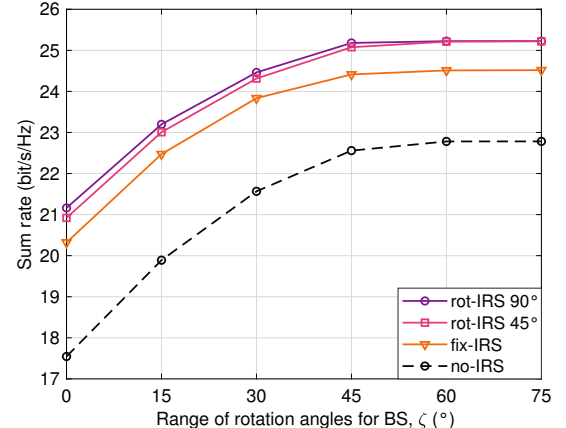


Fig. 7. Sum rate versus the number of communication users under $p^R = p^B = 2$ with $N = 6 \times 6$, $M = 2 \times 2$, and $P = 30$ dBm.

and fully fixed benchmarks. In summary, combining array scaling with geometric adaptation is effective for one-dimensional arrays in ISAC systems, especially with directional arrays with practical radiation patterns.

Figs. 6 investigate user scaling for a 2×4 BS array with fixed transmit power $P_B = 22$ dBm. The sum rate increases with the number of users due to multiuser multiplexing gains, but the growth gradually slows as the system becomes more interference-limited and the available spatial degrees of freedom must be shared between user separation and sensing beampattern shaping. The Rot-BS+Rot-RIS scheme consistently delivers the highest sum rate, demonstrating that joint geometry control is especially beneficial in the multiuser regime, whereas partial rotation or fixed architectures suffer from stronger interference and tighter sensing constraints.

Fig. 7 illustrates the impact of the maximum BS rotation range ζ on the achievable sum rate for different RIS array rotation ranges. As ζ increases, the sum rate of all schemes improves and gradually saturates, since a larger rotation range provides more geometric degrees of freedom to steer the BS beams toward the users and away from interference directions. Across the whole range of ζ , both rotatable-RIS configurations significantly outperform the fixed-RIS and no-RIS baselines, confirming that jointly adapting the BS orientation and the RIS reflection direction is highly beneficial. Moreover, the curves

for “rot-IRS 90°” and “rot-IRS 45°” almost coincide once ζ exceeds 30°, indicating that a moderate IRS rotation capability already captures most of the gain brought by passive array rotation, while the BS rotation range remains the dominant factor in leveraging geometric flexibility.

V. CONCLUSION

This paper studied a low-altitude ISAC system with cooperative rotatable active and passive arrays. We considered a downlink transmission where a BS equipped with an active RA serves multiple ground users and senses low-altitude targets in monostatic mode, assisted by a rotatable RIS, i.e., passive RA. To capture the impact of 3D array rotations, we developed a rotation-aware geometry-based multipath channel model in which BS–user, BS–RIS, and RIS–user links are parameterized by path-dependent 3D angles and complex gains, and array rotations jointly affect steering vectors and direction-dependent element gains. On this basis, we formulated a unified design that maximizes the multiuser sum rate under a transmit-power budget, RIS unit-modulus constraints, mechanical rotation limits, and a sensing beampattern MSE constraint. To tackle the resulting highly coupled and non-convex problem, we proposed a penalty-based AO framework that alternately updates the BS ISAC precoder, RIS phase-shift vector, and BS/RIS rotation angles. The BS precoding block is solved via a QT– and MM-aided method, leading to a tractable QCQP; the RIS block is handled on the complex-circle manifold using an RGD algorithm; and the rotation block is optimized via PGD with Barzilai–Borwein step sizes and Armijo backtracking. Extensive simulations under LAWN-inspired 3D geometries showed that the proposed jointly rotatable BS–RIS architecture achieves significant sum-rate gains over fixed or partially rotatable baselines while satisfying stringent sensing MSE requirements, with the advantages further amplified with directional antennas.

REFERENCES

- [1] G. Sun *et al.*, “Generative artificial intelligence for beamforming in low-altitude economy,” *IEEE Wireless Commun.*, early access, doi: 10.1109/MWC.2025.3623988.
- [2] Y. Wang *et al.*, “Toward realization of low-altitude economy networks: Core architecture, integrated technologies, and future directions,” *IEEE Trans. Cognit. Commun. Netw.*, vol. 11, no. 5, pp. 2788–2820, Oct. 2025.
- [3] J. Li *et al.*, “Aerial secure collaborative communications under eavesdropper collusion in low-altitude economy: A generative swarm intelligent approach,” *IEEE Trans. Mobile Comput.*, early access, doi: 10.1109/TMC.2025.3633953.
- [4] Y. Zeng, Q. Wu, and R. Zhang, “Accessing from the sky: A tutorial on UAV communications for 5G and beyond,” *Proc. IEEE*, vol. 107, no. 12, pp. 2327–2375, Dec. 2019.
- [5] F. Liu *et al.*, “Integrated sensing and communications: Toward dual-functional wireless networks for 6G and beyond,” *IEEE J. Sel. Areas Commun.*, vol. 40, no. 6, pp. 1728–1767, Jun 2022.
- [6] A. Liu *et al.*, “A survey on fundamental limits of integrated sensing and communication,” *IEEE Commun. Surveys Tut.*, vol. 24, no. 2, pp. 994–1034, Secondquarter 2022.
- [7] D. Gesbert *et al.*, “Shifting the MIMO Paradigm,” *IEEE Signal Process. Mag.*, vol. 24, no. 5, pp. 36–46, Sep. 2007.
- [8] E. G. Larsson *et al.*, “Massive MIMO for next generation wireless systems,” *IEEE Commun. Mag.*, vol. 52, no. 2, pp. 186–195, Feb. 2014.
- [9] Q. Wu *et al.*, “Intelligent surfaces empowered wireless network: Recent advances and the road to 6G,” *Proc. IEEE*, vol. 112, no. 7, pp. 724–763, Jul. 2024.
- [10] Q. Wu and R. Zhang, “Towards smart and reconfigurable environment: Intelligent reflecting surface aided wireless network,” *IEEE Commun. Mag.*, vol. 58, no. 1, pp. 106–112, Jan. 2020.
- [11] Q. Wu, *et al.*, “Intelligent reflecting surface-aided wireless communications: A tutorial,” *IEEE Trans. Commun.*, vol. 69, no. 5, pp. 3313–3351, May 2021.
- [12] A. M. Elbir *et al.*, “The rise of intelligent reflecting surfaces in integrated sensing and communications paradigms,” *IEEE Netw.*, vol. 37, no. 6, pp. 224–231, Nov. 2023.
- [13] M. Hua *et al.*, “Joint Active and Passive Beamforming Design for IRS-Aided Radar-Communication,” *IEEE Tran. Wireless Commun.*, vol. 22, no. 4, pp. 2278–2294, Apr 2023.
- [14] Y. Guo *et al.*, “Joint beamforming and power allocation for RIS aided full-duplex integrated sensing and uplink communication system,” *IEEE Trans. Wireless Commun.*, vol. 23, no. 5, pp. 4627–4642, May 2024.
- [15] L. Zhu, W. Ma, and R. Zhang, “Movable antennas for wireless communication: Opportunities and challenges,” *IEEE Commun. Mag.*, vol. 62, no. 6, pp. 114–120, June 2024.
- [16] L. Zhu, *et al.*, “Movable-antenna enhanced multiuser communication via antenna position optimization,” *IEEE Trans. Wireless Commun.*, vol. 23, no. 7, pp. 7214–7229, July 2024.
- [17] Y. Guo *et al.*, “Movable antenna enhanced networked integrated sensing and communication system,” *IEEE Trans. Wireless Commun.*, early access, doi: 10.1109/TWC.2025.3619214.
- [18] Y. Guo *et al.*, “Cramér–Rao bound optimization for fluid antenna-empowered integrated sensing and uplink communication system,” arXiv preprint: 2510.25246, <https://arxiv.org/abs/2510.25246>, 2025.
- [19] H. Wang, Q. Wu, and W. Chen, “Movable antenna enabled interference network: Joint antenna position and beamforming design,” *IEEE Wireless Commun. Lett.*, vol. 13, no. 9, pp. 2517–2521, Sept. 2024.
- [20] Y. Gao, Q. Wu, and W. Chen, “Joint transmitter and receiver design for movable antenna enhanced multicast communications,” *IEEE Trans. Wireless Commun.*, vol. 23, no. 12, pp. 18186–18200, Dec. 2024.
- [21] Z. Zheng, Q. Wu, W. Chen and G. Hu, “Two-timescale design for movable antenna-enabled multiuser MIMO systems,” in *IEEE Transactions on Communications*, vol. 73, no. 11, pp. 10554–10571, Nov. 2025.
- [22] Q. Wu *et al.*, “Integrating movable antennas and intelligent reflecting surfaces (MA-IRS): Fundamentals, practical solutions, and ISAC,” *IEEE Wireless Commun.*, early access, doi: 10.1109/MWC.2025.3623970.
- [23] H. Wang *et al.*, “Reconfigurable airspace: Synergizing movable antenna and intelligent surface for low-altitude ISAC networks,” arXiv preprint: 2511.10310, <https://arxiv.org/abs/2511.10310>, 2025.
- [24] B. Zheng, Q. Wu, T. Ma, and R. Zhang *et al.*, “Rotatable antenna enabled wireless communication: Modeling and optimization,” arXiv preprint: 2501.02595, <https://arxiv.org/abs/2501.02595>, 2025.
- [25] X. Peng *et al.*, “Rotatable antenna enabled spectrum sharing: Joint antenna orientation and beamforming design,” arXiv preprint: 2509.19912, <https://arxiv.org/abs/2509.19912>, 2025.
- [26] K. Shen and W. Yu, “Fractional Programming for Communication Systems—Part I: Power Control and Beamforming,” *IEEE Trans. Signal Process.*, vol. 66, no. 10, pp. 2616–2630, May 15, 2018.
- [27] Y. Sun, P. Babu and D. P. Palomar, “Majorization-minimization algorithms in signal processing, communications, and machine learning,” *IEEE Trans. Signal Process.*, vol. 65, no. 3, pp. 794–816, 1 Feb. 1, 2017.
- [28] N. Boumal *et al.*, “Manopt, a Matlab toolbox for optimization on manifolds,” *J. Mach. Learn. Res.*, vol. 15, no. 42, pp. 1455–1459, 2014. [Online]. Available: <https://www.manopt.org>
- [29] C. Liu and N. Boumal, “Simple Algorithms for Optimization on Riemannian Manifolds with Constraints,” *Appl. Math. Optim.*, 82, 949–981, 2020. <https://doi.org/10.1007/s00245-019-09564-3>
- [30] J. Nocedal and S. J. Wright, “Fundamentals of algorithms for nonlinear constrained optimization,” *Numerical Optimization*. NewYork, NY: SpringerNewYork, 2006, pp.421–447.